ROYAL SOCIETY OF CHEMISTRY

EES Catalysis

REVIEW ARTICLE

View Article Online
View Journal | View Issue

Check for updates

Cite this: *EES Catal.*, 2025, **3**, 359

Aspects in cell design for H_2O_2 electrosynthesis and its integration in tandem systems†

Wenhao Chen, Chang Sun and Wenchao Sheng *

Received 28th October 2024,
Accepted 31st January 2025

DOI: 10.1039/d4ey00232f

rsc.li/eescatalysis

Hydrogen peroxide (H_2O_2) is an environment-friendly oxidant with wide applications in daily life and the chemical industry. The electrochemical production of H_2O_2 through the two-electron oxygen reduction ($2e^-$ ORR) process has the advantages of high safety, high energy-efficiency, and environmental sustainability. Prior investigations predominantly concentrated on the intrinsic properties of the catalysts, rather than the performance of the electrodes in real reactors. In this review, the aspects in cell design for H_2O_2 electrosynthesis will be discussed, including the surface and interface modifications for the carbon electrodes, and the reaction system design for practical H_2O_2 electrosynthesis, highlighting the critical needs in electrodes and reactors to enhance $2e^-$ ORR performance. Additionally, this review will cover the applications of $2e^-$ ORR integrated tandem systems for chemical synthesis. Finally, current challenges and prospects for future studies in H_2O_2 electrosynthesis will be presented.

Broader context

Hydrogen peroxide (H_2O_2) is a versatile green oxidizing agent with growing demand in the global market for its extensive applications in medical disinfection, pulp bleaching, chemical synthesis, wastewater treatment *etc.* The electrocatalytic two-electron oxygen reduction reaction ($2e^-$ ORR) is an environment-friendly and energy-efficient alternative approach compared to the traditional energy-intensive anthraquinone process, owing to its advantages of on-site production, green feedstocks from air, and non-polluting H_2O as the only byproduct. With the development of high-performance $2e^-$ ORR catalysts, research focuses have been gradually geared towards practical reactors to facilitate scaled-up H_2O_2 electrosynthesis. This review presents a comprehensive overview of cell design for H_2O_2 electrosynthesis and its integration in tandem systems for chemical synthesis, emphasizing key aspects such as electrode surface wettability management, interface microenvironment modification, design of reactor key components, practical challenges, and the integration of the $2e^-$ ORR in tandem systems for synthesizing value-added chemicals. The information and insights delivered in this review could be potentially adopted for other electrocatalytic reactions such as carbon dioxide reduction and nitrogen reduction reactions.

State Key Laboratory of Pollution Control and Resource Reuse, College of Environmental Science and Engineering, Tongji University, Shanghai Institute of Pollution Control and Ecological Security, Shanghai 200092, P. R. China. E-mail: wsheng@tongji.edu.cn

† Electronic supplementary information (ESI) available. See DOI: https://doi.org/10.1039/d4ey00232f

Wenhao Chen

Wenhao Chen is currently a MSc candidate under the supervision of Prof. Wenchao Sheng in the College of Environmental Science and Engineering at Tongji University. He received his BSc degree from East China University of Science and Technology in 2022, with a major in safety engineering. His current research mainly focuses on the electrode design and device applications of oxygen reduction reactions.

Chang Sun

Chang Sun is currently a PhD candidate under the supervision of Prof. Wenchao Sheng in the College of Environmental Science and Engineering at Tongji University. She received her BSc degree from Northeast Forestry University in 2019, majoring in environmental science. Her current research mainly focuses on the fundamental science in oxygen electrocatalysis and applications of renewable energy technologies.

1 Introduction

Hydrogen peroxide (H_2O_2) is one of the 100 most important chemical compounds.[1] As an environment-friendly oxidant, H_2O_2 has a growing global market demand for its extensive applications in medical disinfection, pulp bleaching, chemical synthesis, wastewater treatment, *etc.*[2–5] The industrial production of H_2O_2 primarily relies on the conventional energy-intensive anthraquinone (AQ) process (~95%), which produces substantial amounts of waste organic pollutants (5,6,7,8-tetrahydroanthrahydroquinone *etc.*) in addition to carbon emissions, posing a severe risk to water environment safety. Besides, the high-concentration H_2O_2 (70 wt%) produced through the AQ process presents potential safety risks in transportation.[6]

The electrochemical synthesis of H_2O_2 based on the two-electron oxygen reduction reaction ($2e^-$ ORR), which selectively converts O_2 to H_2O_2, with H_2O as the only by-product, offers a green, safe and energy-efficient alternative to the conventional anthraquinone process.[7] Recently, numerous catalysts have been developed for the $2e^-$ ORR, including precious metals, non-precious metals and carbon materials.[8–10] Precious metal catalysts, such as $PtHg_4$ alloy[11] and Pt-based sulfides, selenides and phosphides ($PtS_{1.38}$,[12] Se_2-Pt,[13] and PtP_2[14]), are regarded as the benchmark catalysts for the $2e^-$ ORR due to their outstanding electrocatalytic performance. The high cost and scarcity of precious metal catalysts, however, limit their large-scale applications. In the realm of non-precious metal catalysts, despite their intrinsic instability compared to precious metals, recent innovations of nanostructured materials have resulted in various electrocatalysts with comparable $2e^-$ ORR performance, including Co and Ni based sulfides and selenides ($NiSe_2$[15] and sc-$CoSe_2$[16]), as well as single-atom and dual-atoms catalysts (Ni-N_3S,[17] Co_1-NBC,[18] Co_2-DAC,[19] and Coln-NC[20]). In addition, recent studies show that metal-free carbon-based catalysts with adjustable electronic structures, good electrical conductivity and stable chemical properties have great potential in H_2O_2 electrosynthesis. Various strategies such as heteroatom doping, defect engineering, and structural engineering have been developed and summarized previously.[10,21,22]

Beyond advancing electrocatalytic materials, the design and optimization of the $2e^-$ ORR system is equally important for highly-efficient H_2O_2 electrosynthesis. Recent studies have underscored the importance of electrode surface/interface microenvironment modification and reactor configuration innovations to accelerate the reaction kinetics and H_2O_2 selectivity.[23,24] It was revealed that the $2e^-$ ORR performance can be influenced by surface wettability,[25] interface proton concentration,[26] and interfacial electric fields.[27] For instance, electrode wettability management is found to be important for the formation of three-phase interfaces (TPIs), which not only shortens the O_2 diffusion path distance from ~50 μm to ~50 nm to reach the active sites,[28] but also avoids further reduction of H_2O_2 in the catalytic layer.[29] Improper wettability management, such as excessive hydrophobicity, would have negative impacts. In terms of reactor configuration innovations, gas diffusion electrode (GDE) based reactors such as flow-cells, solid–electrolyte cells, and membrane electrode assembly cells have been increasingly reported for different application scenarios. The optimization of the key components of a reactor such as the gas flow channel and electrolyte compartments is critical to enhance the overall reactor performance. For example, the rational design of gas flow channels in a reactor can facilitate O_2 transfer by vertical diffusion, increasing the H_2O_2 production rate.[30,31] Meanwhile, GDE-based reactors may encounter additional challenges in real-world applications, such as the Joule heating effect,[32] electrode fouling issue,[33] and membrane degradation issue, which have not been fully understood yet.

While electro-synthesized H_2O_2 can be directly used in traditional downstream applications, it's *in situ* coupling with tandem systems for value-added chemical synthesis has attracted increasing attention lately. The high concentration of H_2O_2 near the electrode surface can be used to accelerate the synthesis of high-purity chemicals, such as ethylene epoxidation to produce ethylene glycol.[34] Besides, the *in situ* generated reactive oxygen species (ROS) from H_2O_2 has also been utilized to activate inert reactants such as methane (CH_4) and nitrogen (N_2).[35,36] Hitherto, no comprehensive analysis and review have focused on the optimization of the $2e^-$ ORR system and its integration in tandem systems for high-value chemical synthesis.

In this review, we summarize the latest advances in practical reaction systems for H_2O_2 electrosynthesis. As illustrated in Fig. 1, the management of surface wettability (①) and interface microenvironment (②) will be discussed in section three, emphasizing the advantages of electrodes with appropriate hydrophobicity, as well as the effects of modifying the interface proton concentration and electric field. Design of reactor key components (③) and reactor configuration (④) will be reviewed in section four, focusing on energy-producing and energy-consuming modes; the challenges and mitigation measures in real-world electrosynthesis will also be discussed. In section five, we will introduce applications of $2e^-$ ORR integrated

Wenchao Sheng

Wenchao Sheng is currently a professor in the College of Environmental Science and Engineering at Tongji University. She obtained her BSc and MSc from the Department of Chemistry at Tongji University, and her PhD from the Department of Chemistry at MIT. After conducting postdoctoral research at the University of Delaware and Columbia University, she joined the faculty of the CESE at Tongji University. Her research interests include fundamental aspects of electrocatalysis in renewable energy storage and conversion technologies, electrochemical synthesis of high-value chemicals, and synthesis and characterization of nanostructured materials for energy applications.

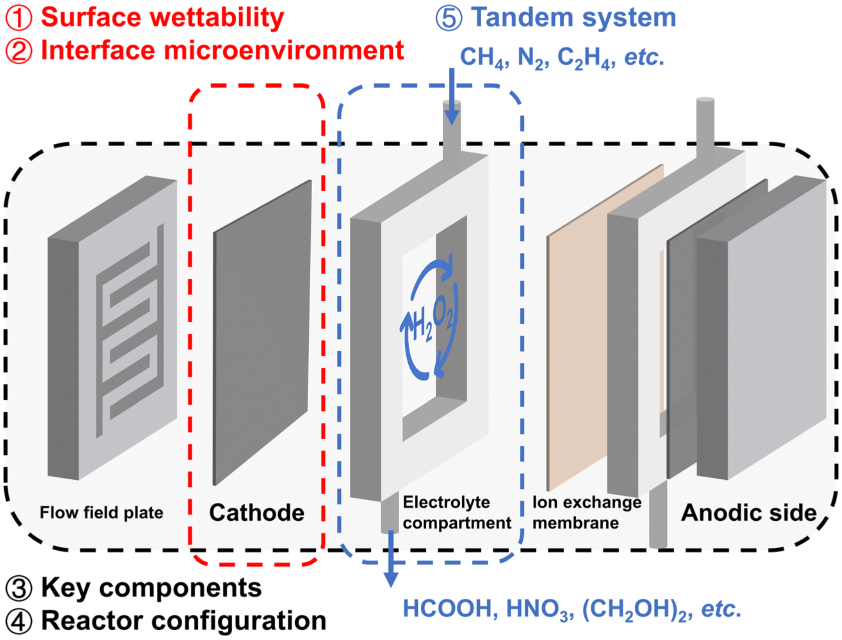

Fig. 1 Schematic illustration of the reactor design for H_2O_2 electrosynthesis and its integration in tandem systems. This review covers the four subtopics (1)–(4) in reactor design and (5) 2e$^-$ ORR integrated tandem systems for chemical synthesis.

tandem systems for chemical synthesis (⑤), and explore the H_2O_2 concentration effect and the ROS effect, highlighting the promising application potential of *in situ* generated H_2O_2.

2 Fundamentals of electrochemical synthesis of H_2O_2 *via* the ORR

The oxygen reduction reaction (ORR) is a complex multi-electron transfer process, following either a four-electron pathway to produce H_2O (acid in eqn (1) and base in eqn (2)) or a two-electron pathway leading to the production of H_2O_2 (acid in eqn (3) and base in eqn (4)). The thermodynamic equilibrium potentials are *versus* the reversible hydrogen electrode (RHE).

$$O_2 + 4H^+ + 4e^- \rightarrow 2H_2O \quad E^0 = 1.23\ \text{V} \tag{1}$$

$$O_2 + 2H_2O + 4e^- \rightarrow 4OH^- \quad E^0 = 1.23\ \text{V} \tag{2}$$

$$O_2 + 2H^+ + 2e^- \rightarrow H_2O_2 \quad E^0 = 0.70\ \text{V} \tag{3}$$

$$O_2 + H_2O + 2e^- \rightarrow HO_2^- + OH^- \quad E^0 = 0.74\ \text{V} \tag{4}$$

Note that in alkaline electrolyte solutions (pH > 11.6), the product of the two-electron pathway changes from H_2O_2 to HO_2^-; the thermodynamic equilibrium potential changes accordingly.

Fig. 2a illustrates the electrocatalytic 2e$^-$ ORR process, including the mass transfer of O_2 from the bulk electrolyte to the electrode surface, adsorption of O_2 at the electrode surface, electrocatalytic reduction of O_2 to H_2O_2, desorption of H_2O_2, and the mass transfer of H_2O_2 back to the bulk electrolyte. The adsorption of O_2, charge transfer at the interface, and desorption of H_2O_2 are directly linked to the catalyst performance, while the mass transfer of both O_2 and H_2O_2 is primarily influenced by the reaction reactor configurations.

ORR processes involve multiple electron and proton transfers, and several reaction intermediates (Fig. 2b). O_2 can be fully reduced to H_2O through the dissociative pathway or reduced to H_2O_2 through the associative pathway. In the associative pathway, O_2 is reduced to form the *OOH intermediate first (eqn (5)), which is subsequently reduced to generate H_2O_2 (eqn (6)). Notably, the *OOH intermediate can also dissociate, and is consequently reduced to H_2O (eqn (7)–(9)). Besides, H_2O_2 can also be further reduced to form H_2O (H_2O_2RR), as shown in eqn (10).

$$O_2 + {*} + H^+ + e^- \rightarrow {*}OOH \tag{5}$$

$${*}OOH + H^+ + e^- \rightarrow H_2O_2 + {*} \tag{6}$$

$${*}OOH + H^+ + e^- \rightarrow H_2O + {*}O \tag{7}$$

$${*}O + H^+ + e^- \rightarrow {*}OH \tag{8}$$

$${*}OH + H^+ + e^- \rightarrow H_2O + {*} \tag{9}$$

$$H_2O_2 + 2H^+ + 2e^- \rightarrow 2H_2O \tag{10}$$

The 2e$^-$ ORR mechanism highlights the crucial role of the *OOH intermediate; thus, the binding energy of ΔG_{*OOH} has been generally accepted as the descriptor for the 2e$^-$ ORR. Fig. 2c presents the volcano plot of the 2e$^-$ ORR on carbon catalysts with various oxygen functional groups. Catalysts on the right branch exhibit weak binding to *OOH, making it difficult for *OOH formation, while the catalysts on the left bind to *OOH too strongly, leading to O–O bond cleavage and ultimately forming H_2O. Catalysts with the optimal *OOH binding energy, favoring *OOH formation and further desorption, exhibit an ideal 2e$^-$ ORR performance.

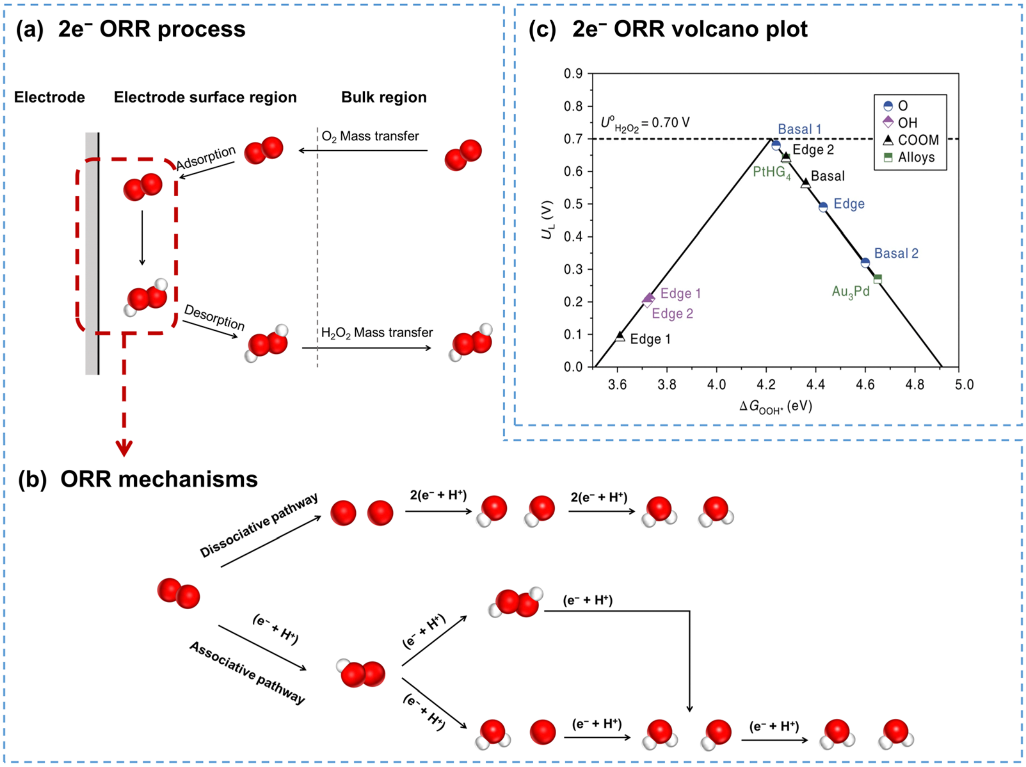

Fig. 2 (a) Schematic of the 2e⁻ ORR process; (b) schematic of ORR mechanisms including dissociative and associative pathways; (c) calculated 2e⁻ ORR volcano plot, with the limiting potential plotted as a function of ΔG_{*OOH}, reprinted with permission from ref. 37. Copyright 2018, Springer Nature.

Selectivity, activity, and stability are the key parameters for evaluating 2e⁻ ORR catalysts. For fundamental studies, the rotating ring-disk electrode (RRDE) is commonly used, wherein O_2 is reduced at the disk electrode, and the produced H_2O_2 will be detected at the Pt-ring electrode. The H_2O_2 molar selectivity can be calculated using eqn (11).

$$H_2O_2\ (\%) = \frac{|i_R/N|}{|i_R/N| + |i_D|} \times 200 \tag{11}$$

where i_R is the ring current, N is the collection efficiency, and i_D is the disk current.

Faraday efficiency (FE), is also an important parameter to evaluate H_2O_2 selectivity, if the energy consumption is the major concern (eqn (12)).[38]

$$H_2O_2FE\ (\%) = \left|\frac{i_R/N}{i_D}\right| \times 100 \tag{12}$$

The H_2O_2 selectivity data obtained using RRDE cannot accurately reflect the selectivity in actual reactors, such as H-cells and flow-cells. The discrepancy arises because H_2O_2 can be rapidly transferred and detected on RRDE, while in actual reactors, the H_2O_2 generated on the electrode surface may proceed with further reduction before detection, resulting in a lower detected selectivity.[6] Typically, the FE of H_2O_2 in actual reactors (λ_{FE}) is calculated using titration and/or UV-vis spectrophotometry, following eqn (13).

$$\lambda_{FE}\ (\%) = \frac{2CVF}{Q} \times 100 \tag{13}$$

where C, V, F and Q are the cumulative concentration of H_2O_2 (mol L^{-1}), total electrolyte volume (L), Faraday constant (96 485 C mol^{-1}) and total electric charge consumed (C) respectively.

The 2e⁻ ORR activity of catalysts can be compared using onset potential and overpotential. Typically, the onset potential is defined as the potential at which the ring current density reaches 0.1 mA cm^{-2}. Catalyst stability can be evaluated by comparing the 2e⁻ ORR performance changes before and after the accelerated durability test, or the current density decline during the chronoamperometry test.[39] The Pt-ring electrode should be cleaned in a timely fashion, since its surface could be oxidized during the stability test, making the quantification of H_2O_2 inaccurate.[40]

3 Carbon electrode surface wettability and interface microenvironment

3.1 Carbon electrode surface wettability management

The management of electrode surface wettability has garnered increasing attention with the continuous development of electrocatalytic reaction systems, especially for reactions involving gaseous reactants or products, for which the optimization of surface wettability is essential. The interaction between gases, electrolytes and catalysts significantly influences the performance of those gas-involving reactions.

3.1.1 Fundamentals in the management of surface wettability. In general, the electrode surface can exhibit three distinct wetting states when in contact with the electrolyte:[41]

the Wenzel state, when the electrode is fully wetted by the electrolyte; the Cassie state, when the electrode remains completely non-wetted by the electrolyte; the Wenzel–Cassie coexistent state for the intermediate condition (Fig. 3a). Matching the appropriate electrode wetting state for a specific reaction type is critical for accelerating the reaction rate.[42–44]

Gas-involving electrocatalytic reactions include gas-evolution reactions (GERs) and gas-consuming reactions (GCRs). For GERs, most studies focus on adjusting the electrode surface to the Wenzel state, which facilitates the timely removal of gas bubbles generated during the reaction due to its strong hydrophilicity, and allows full recovery of active sites on the electrode surface.[47–49] For GCRs, the surface wettability must be carefully tailored due to the varying diffusion paths of gaseous reactants in reaction systems.

The 2e$^-$ ORR is a typical gas-consuming reaction. When O_2 diffuses to the electrode surface in the form of dissolved oxygen, hydrophilic electrodes in the Wenzel state are considered advantageous, and are commonly used in fundamental research systems like RRDE and H-cells.[25] For instance, a honeycomb carbon nanofiber (HCNF) electrode with a nearly zero contact angle could increase the H_2O_2 selectivity from 65% to 97% in the RRDE system.[50] Recently, by heat-treating the porous carbon materials (HGC) at different temperatures, You *et al.*[51] found that HGC_{550} treated at 550 °C with the highest hydrophilicity showed superior 2e$^-$ ORR performance compared with other electrodes with relatively low hydrophilicity. Further H-cell experiments demonstrated that HGC_{550} operated stably with 95% H_2O_2 selectivity for 12 hours, achieving a cumulative H_2O_2 concentration of up to 4000 ppm, among the top performances using the H-cell configuration.

The O_2 mass transfer in the GDE system is more complicated and noteworthy. Initially, gaseous O_2 diffuses through the

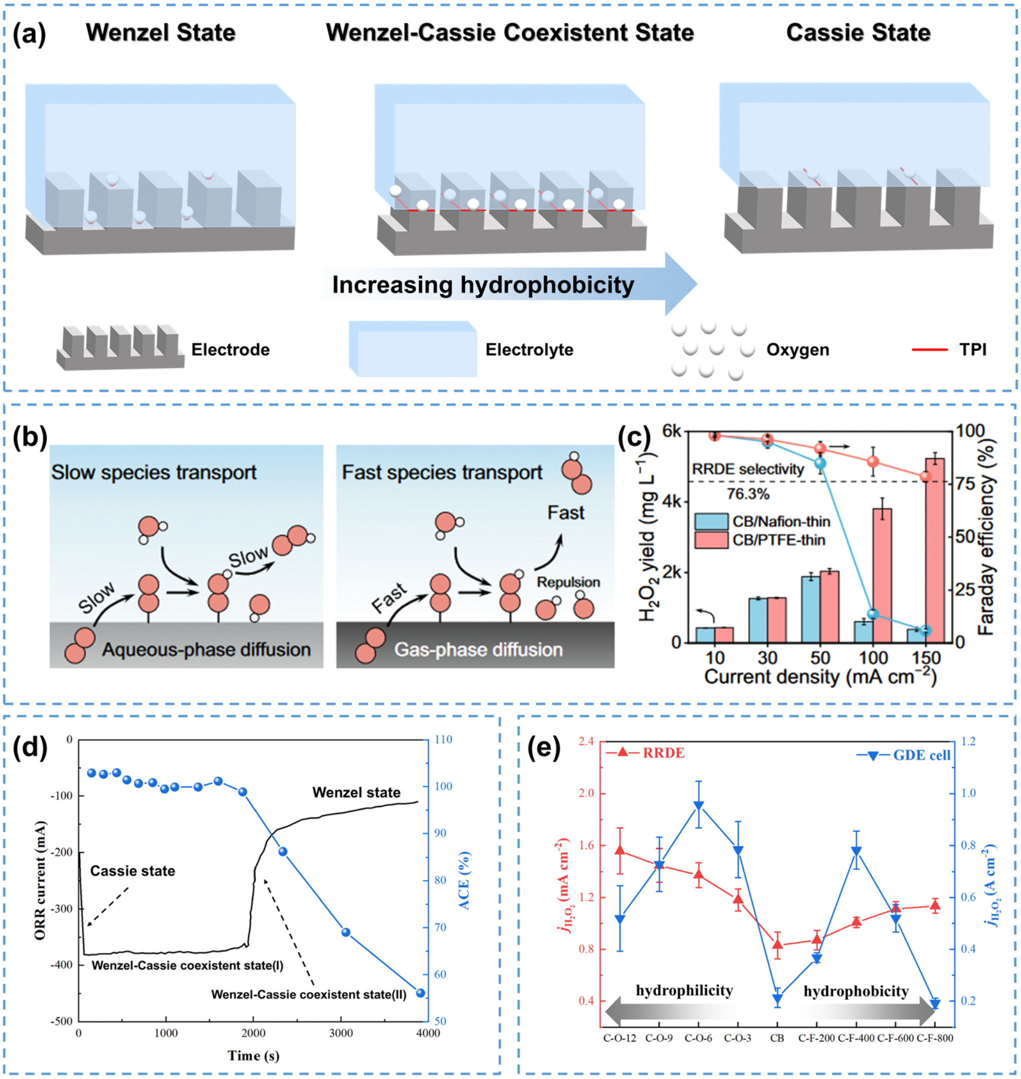

Fig. 3 (a) Electrode surface wetting states: Wenzel state, Wenzel–Cassie coexistent state, and Cassie state, adapted from ref. 41; (b) schematic of species transfer at the electrode scale, and (c) H_2O_2 production performance of CB/Nafion-thin and CB/PTFE-thin electrodes at different current densities; (b) and (c) are reprinted with permission from ref. 29 copyright 2024, Springer Nature; (d) the evolution of electrode surface wetting states and apparent current efficiency (ACE) during the ORR process; data were taken from ref. 45; (e) the H_2O_2 current density at 0.60 V measured in both RRDE and GDE cells at different wetting states; data were taken from ref. 46.

GDE substrate, and further reaches the active sites in the catalyst layer through the gas phase and/or aqueous diffusion (diffusion in gaseous oxygen and/or dissolved oxygen) depending on the wettability of the catalyst layer.[46] When the GDE surface is fully hydrophilic (Wenzel state, left in Fig. 3b),[29] gas channels are easily flooded by the electrolyte, and O_2 can only diffuse in the dissolved form, which results in a sluggish reaction rate because the diffusion coefficient of dissolved oxygen is three orders of magnitude slower than that of gaseous oxygen in GDE.[52,53] On the other hand, when the surface is in a fully hydrophobic Cassie state, proton transfer from the electrolyte to the electrode surface will be hindered, which is detrimental to the reaction. Therefore, the GDE surface should be neither excessively hydrophilic nor hydrophobic. When the GDE surface is in a Wenzel–Cassie coexistent state, a gas–solid–liquid three-phase boundary is achieved on the electrode surface, facilitating both O_2 and proton transfer, and in turn the efficient production of H_2O_2 (right in Fig. 3b).[29,54,55] In addition, wettability management is also decisive for the efficient mass transfer of the produced H_2O_2. The reactive electron flux distribution on the hydrophilic electrode surface is in the catalytic layer immersed in the electrolyte, which can easily induce unwanted HER and H_2O_2RR; when the electrode is in a Wenzel–Cassie coexistent state, the reactive electron flux will be distributed on the three-phase boundary to perform the 2e$^-$ ORR. As evidenced in Fig. 3c, the H_2O_2 yield of the hydrophilic CB/Nafion-thin electrode initially increased and then decreased with increasing current density, while the yield of the CB/PTFE-thin electrode in the Wenzel–Cassie coexistent state increased continuously, which was attributed to the fast mass transfer rate of the produced H_2O_2.[29] The evolution of electrode surface wettability was experimentally observed by Xia *et al.*[45] As shown in Fig. 3d, the electrode surface in the Cassie state exhibited low current during the first 100 seconds. The electrode surface quickly transitioned to a Wenzel–Cassie coexistent state, which exhibited the highest activity and selectivity, lasting for nearly 2000 seconds. As the reaction further progressed, the electrode surface shifted to a Wenzel state, resulting in a sharp drop in current from 400 mA to 100 mA, and a reduction in apparent current efficiency (ACE) from 100% to 55%, which was attributed to the flooding by the electrolyte.

Generally, the carbon electrode wettability can be adjusted by controlling the surface functional groups and/or doping with heteroatoms. Note that the intrinsic activity will also be altered simultaneously, which should be considered when adjusting the electrode wettability. By modifying the hydrophilicity/hydrophobicity of carbon black (CB) electrodes, Xing *et al.*[46] found that the CB electrodes exhibited different trends for their surface hydrophilicity/hydrophobicity in RRDE and GDE configurations (Fig. 3e). In RRDE, the activity of CB increased significantly with increasing hydrophilicity, while increasing its hydrophobicity hardly affected the activity. Nevertheless, the performance of GDEs after both hydrophilic and hydrophobic modifications exhibited a double volcano (M-shaped) correlation with the hydrophilicity/hydrophobicity of CB. Both F-doping and O-doping affected the 2e$^-$ ORR performance of carbon electrodes by influencing the number of TPIs. For the hydrophobically modified electrode (F-doped), the number of TPIs initially increased with increasing hydrophobicity, while excessive hydrophobicity would decrease the number of solid–liquid interfaces, thus decreasing the current density. For a hydrophilic modified electrode (O-doped), the activity initially increased due to increased intrinsic activity and increased solid–liquid interfaces, receiving more dissolved oxygen from the electrolyte. However, further hydrophilic treatment leads to electrode flooding, reducing the TPIs. Further stability tests showed that the hydrophobically optimized electrode (C-F-400) maintained a stable current density of 200 mA cm^{-2} and a FE of 90% for at least 12 hours, whereas the hydrophilic optimized electrode (C-O-6h) exhibited an 80% decrease in current density within 4 hours, due to severe electrode flooding.

The aforementioned studies suggest that appropriate hydrophobic modification is preferred to enhance the overall 2e$^-$ ORR performance when using the GDE system. In general, there are two main strategies for hydrophobic modification of electrodes: using hydrophobic polymers and increasing the roughness of the electrode surface.[25,56]

3.1.2 Managing surface wettability using hydrophobic polymers.

Typically, GDE is prepared by dispersing the powder catalyst and binder in water or isopropyl alcohol to create a catalyst ink, and depositing the ink on the gas diffusion layer (GDL) by drop coating, spraying or immersion. As polytetrafluoroethylene (PTFE) has exceptional hydrophobicity, high chemical stability and low cost,[25] it is commonly incorporated into the GDE fabrication to modify the wettability of the carbon electrode. For instance, Zhang *et al.*[57] pretreated the catalyst layer with PTFE, and fabricated an air diffusion electrode with stable TPIs (Fig. 4a), which demonstrated a 5.7 times higher O_2 diffusion coefficient than that of untreated GDEs, enabling efficient and stable H_2O_2 production (101.67 mg h^{-1} cm^{-2}) with a high O_2 utilization efficiency (44.5%–64.9%).

When subjected to heat treatment above 350 °C, PTFE will melt and bond with the carbon materials, which further enhances the hydrophobicity of carbon electrodes. By calcinating PTFE-containing GDE at 360 °C, Yu *et al.*[61] successfully improved the H_2O_2 yield to 472.9 mg L^{-1}. Scanning electron microscope images showed that the carbon fibers were tightly bonded with PTFE, and contact angle tests confirmed increased hydrophobicity.

It has to be pointed out that, the calcination process of PTFE will potentially block the active sites since PTFE can encapsulate carbon materials at high temperatures, and its agglomeration can obstruct the pore structure of GDE.[62] To solve these issues, PTFE nanoparticles (NPs) are directly used without heat treatment to enhance the hydrophobicity of carbon electrodes and prevent active site blockage. Hu *et al.*[58] physically mixed PTFE NPs with carbon nanotubes (CNT-NH_2) to create hydrophobic electrodes. As illustrated in Fig. 4b, the electrode surface without PTFE NPs was in a fully wetted Wenzel state, where O_2 could only participate in the form of dissolved oxygen. When the PTFE mass ratio increased to 60%, the electrode surface converted to a completely non-wetted Cassie state, thus

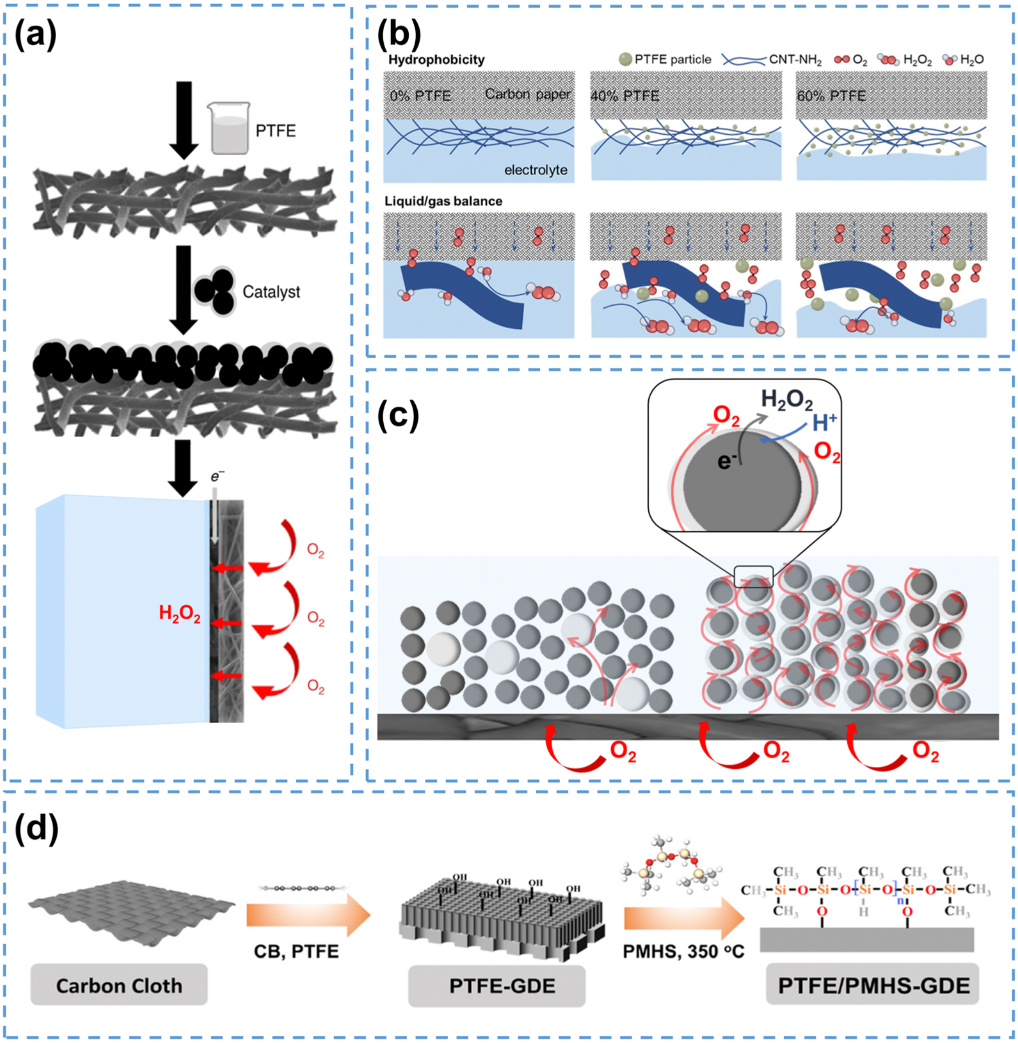

Fig. 4 (a) The fabrication process of hydrophobic air diffusion electrodes, reprinted with permission from ref. 57, copyright 2020, Springer Nature; (b) schematic of the CNT-NH_2/PTFE electrodes with different PTFE mass loading, reprinted with permission from ref. 58, copyright 2023, Wiley-VCH; (c) schematic of the short-range effect of PTFE NPs and optimization strategy using a thin and intact polymer layer on the catalyst surface, adapted from ref. 59; (d) the PTFE/PMHS-GDE fabrication process, reprinted with permission from ref. 60, copyright 2024, Elsevier.

hindering the contact between the electrode and electrolyte. When the PTFE mass ratio was 40%, the electrode surface achieved a partially wetted Wenzel–Cassie coexistent state, enabling the formation of TPIs, and thus improving the H_2O_2 production.

Despite its excellent performance in modifying the surface wettability, the addition of PTFE reduces the ionic conductivity, thus hindering the electrocatalytic reaction. To address this issue, Rawah *et al.*[63] incorporated sodium polystyrene sulfonate (AS-4), an anionic conducting polymer, into the PTFE layer, which established an anionic transport channel and enhanced the ionic conductivity, enabling efficient HO_2^- transfer. The modified carbon electrode achieved a current density of 250 mA cm^{-2} at 2.2 V with a H_2O_2 selectivity above 90%.

Another issue associated with PTFE is that the physical mixing of PTFE NPs with carbon catalysts to construct TPIs may have a short-range effect, which may only modify the hydrophobicity of catalyst particles nearby. This phenomenon has been observed in a recent study using the same strategy to construct TPIs for electrochemical reduction of CO_2 (CO_2RR),[59] and the authors suggested that decorating a thin hydrophobic polymer layer on the catalyst surface could enable the hydrophobic modification for all the catalyst particles, and enhance electrocatalytic performance by forming abundant TPIs. This concept can be potentially applied in H_2O_2 electrosynthesis, as illustrated in Fig. 4c. Recently, Xia *et al.*[60] employed a novel molecular engineering strategy by binding polymethylhydrosiloxane (PMHS) onto the catalyst surface to achieve hydrophobic modification of the carbon electrode, which exhibited higher H_2O_2 yield and better stability compared to conventional GDEs (Fig. 4d). Similarly, Wang *et al.*[64] used 1-octadecanethiol (ODT) for surface decoration to prepare a hydrophobic electrode (HMCSs@ODT), which exhibited enhanced 2e⁻ ORR performance. Using hydrophobic polymers offers a general strategy for hydrophobicity management, and further efforts should be focused on developing more stable and environment-friendly hydrophobic polymers for H_2O_2 production.

3.1.3 Managing surface wettability by tuning the electrode microstructure. Microstructural engineering of the electrode surface offers a superior alternative to hydrophobic polymer modification, which enables self-modification of the electrode wettability by altering the surface roughness.[56] This approach fundamentally avoids the use of hydrophobic polymers, preventing potential issues such as active site blockage and reduced ionic conductivity.

The wettability of electrodes is directly linked to the wettability of the catalysts, and electrodes composed of hydrophobic catalysts typically exhibit hydrophobic properties. For instance, Cao *et al.*[65] synthesized a highly hydrophobic N-doped carbon catalyst (NPC) with ZIF-8 as the precursor, which enhanced the gaseous oxygen utilization. Consequently, the NPC electrode maintained a FE of 90% under 250 mA cm^{-2} and operated it stably at 100 mA cm^{-2} for 200 hours, while the hydrophilic treated NPC electrode experienced severe water flooding in less than 10 hours. Another study illustrated that N-doped carbon catalysts with higher porosity possessed better $2e^-$ ORR performance,[66] which probably was also attributed to the higher hydrophobicity.

Considering the high preparation costs of hydrophobic catalysts, it is more practical to engineer microstructures with rough surfaces directly onto the electrode to manage the hydrophobicity. Plasma-enhanced chemical vapor deposition (PECVD) can be used to create carbon structures with precise size and morphology on electrodes,[67–69] which has been well-established and may be suitable for large-scale preparation of hydrophobic electrodes for H_2O_2 electrosynthesis. Wang *et al.*[70] used the PECVD method to grow ordered vertical graphene (VG) arrays on carbon paper, which exhibited enhanced hydrophobicity and $2e^-$ ORR performance compared to those with a disordered graphene electrode, delivering a superior selectivity of 94% and a H_2O_2 yield of 61.3 mg h^{-1} cm^{-2} at 100 mA cm^{-2}. It was reported that subsequent vacuum treatment could lead to the formation of hydrocarbons at the edges of the graphene structure and enhance the hydrophobicity of VG electrodes.[71,72] Zhang *et al.*[73] applied similar methods to prepare a hydrophobic self-supporting GDE, which ensured the formation of TPIs during the electrocatalytic process, exhibiting 97% selectivity and improved $2e^-$ ORR activity (Fig. 5a).

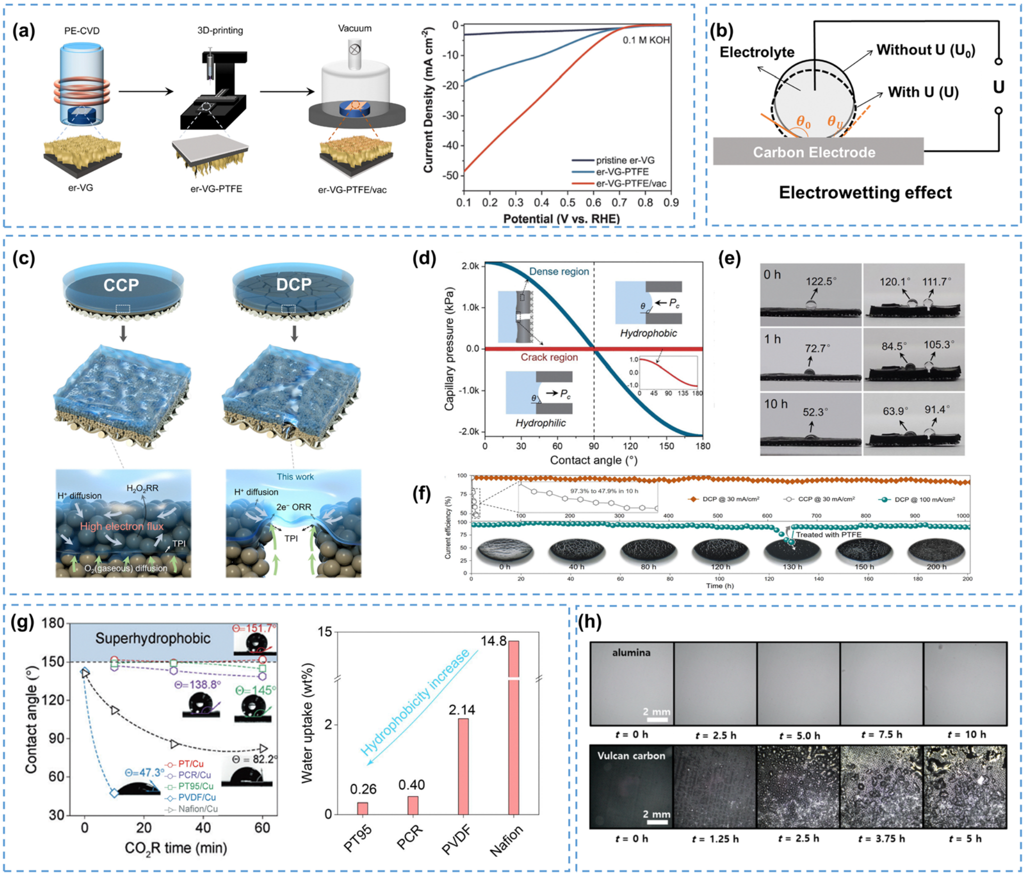

Fig. 5 (a) Schematic of the er-VG-PTFE/vac fabrication process, and the LSVs measured in 0.1 M KOH, reprinted with permission from ref. 73, copyright 2023, Elsevier; (b) schematic of the electrowetting effect, adapted from ref. 74; (c) structurally continuous (CCP) and discontinuous (DCP) CB-PTFE film electrodes, (d) calculated capillary pressure for the dense region and crack region of the DCP surface *vs.* contact angle, (e) contact angles of CCP (left) and DCP (right) electrode surfaces during the reaction, and (f) stability comparison of CCP and DCP electrodes; (c)–(f) are reprinted with permission from ref. 75, copyright 2024, Royal Society of Chemistry; (g) contact angles for five polymer/Cu GDEs at −0.5 A cm^{-2} (left) and water uptake ability of five polymers (right), reprinted with permission from ref. 76, copyright 2024, Springer Nature; (h) flooding behavior comparison of alumina and carbon-based GDLs during electrolysis, reprinted with permission from ref. 77, copyright 2024, American Chemical Society.

Although many strategies have been developed to enhance electrode hydrophobicity, the electrowetting phenomenon, referring to the transition of an electrode surface from a hydrophobic state to a hydrophilic state due to the electric field-driven reduction of solid–liquid surface tension,[74,78] is unavoidable and has often been overlooked. Electrowetting will result in a decreased contact angle on the electrode surface (eqn (14), Fig. 5b),[74] which is more pronounced in catalysts and/or electrodes without intentional hydrophobic modifications, posing a risk of electrode flooding.

$$\cos\theta_U = \cos\theta_0 + \frac{\varepsilon_0\varepsilon_\mathrm{r}}{2d\gamma_\mathrm{LG}}(U - U_0)^2 \qquad (14)$$

Eqn (14) is the Lippmann–Young equation, where θ_U and θ_0 are the contact angles between liquid and solid at U and U_0; ε_0 and ε_r are the absolute dielectric constant in vacuum and the relative dielectric constant of the dielectric; d is the average thickness of the dielectric; γ_LG is the surface tension coefficient at the interface between liquid and gas.

Suppressing electrowetting is crucial for the industrialization of H_2O_2 electrosynthesis, and researchers have mainly focused on the electrode microstructure, polymer coatings, and GDL materials to mitigate this inevitable phenomenon. Recently, Cui *et al.*[75] developed discontinuous CB-PTFE films (DCP) with anti-electrowetting properties, which improved the H_2O_2 production rate compared to traditional continuous CB-PTFE films (CCP), as shown in Fig. 5c. Cracks on the surface of the DCP electrode caused spatial discontinuities that weakened the electric field, thereby reducing the electrowetting effect. The lower capillary pressure in the cracked region (Fig. 5d) prevented the DCP electrode from being excessively hydrophilic or hydrophobic, constructing efficient TPIs. The contact angles of the dense region in both CCP and DCP electrodes were severely dropped from 122.5° to 52.3° and from 120.1° to 63.9°, respectively, exhibiting susceptible electrowetting properties. In contrast, the crack region of the DCP electrode showed stable hydrophobicity after 10 hours of electrolysis (from 111.7° to 91.4°), which further confirmed its excellent anti-electrowetting property (Fig. 5e). No electrode flooding was observed during the 1000-hour stability test for the DCP electrode at 30 mA cm^{-2}, while the CCP electrode was flooded within the initial few hours (Fig. 5f). The overall anti-electrowetting ability of the electrode can also be enhanced by using hydrophobic polymers, as evidenced in previous studies on the CO_2RR.[76,77] As shown in Fig. 5g, the contact angle of the electrode, modified by the most commonly used Nafion, decreased sharply within only 30 min and ended up at 82.2°. Surprisingly, the PT95-modified electrode exhibited super stable hydrophobicity (151.7°), exhibiting excellent anti-electrowetting properties during the CO_2RR. These phenomena may be related to their water uptake abilities (14.8 wt% for Nafion; 0.26 wt% for PT95, shown on the right in Fig. 5g).[76] It was also observed that the inherent conductivity of GDL plays a crucial role in electrowetting (eqn (14)), and materials with high conductivity, *e.g.* carbon, have been proven to be more easily flooded.[79] Recently, Haaring *et al.*[77] replaced the generally used carbon powder with non-conductive dielectric alumina to diminish the electrowetting effect, and found that the alumina GDL exhibited excellent resistance to electrowetting (over 10 hours), whereas the carbon GDL experienced severe flooding within only 2.5 hours (Fig. 5h).

3.2 Carbon electrode interface microenvironment modification

The carbon electrode surface wettability management physically establishes stable TPIs, facilitating efficient O_2 mass transfer and ensuring highly efficient and stable H_2O_2 electrosynthesis. The chemical microenvironment at the electrode–electrolyte interface also affects the activity and selectivity for H_2O_2 electrosynthesis.

The electrocatalytic reaction occurs within the confined nanoscale space between the electrode and electrolyte, known as the electrode–electrolyte interface.[80] The electric double layer (EDL) model, which consists of the inner Helmholtz plane (IHP), outer Helmholtz plane (OHP) and diffusion layer, has been used to describe the electrode–electrolyte interface.[81]

The ions and solvent water molecules adsorbed in the double layer create the EDL microenvironment, which can be optimized to enhance the $2e^-$ ORR performance. The potential of zero charge (PZC) refers to the potential at which an electrode has zero net charge, serving as a key parameter in describing the double-layer structure. When the working potential of the $2e^-$ ORR is higher than the PZC, the electrode becomes positively charged, causing water molecules and anions to aggregate in the IHP due to electrostatic forces, while repelling cations from the electrode interface. Conversely, when the working potential of the $2e^-$ ORR is below the PZC, the electrode carries negative charges, which results in the distribution of water molecules in the IHP with hydrogen atoms in water orienting towards the electrode interface.[82] The high degree of hydration and large hydration radius of alkali metal cations (AMCs) make it difficult to reach the IHP at the electrode–electrolyte interface, and it is generally regarded that the hydrated AMCs will accumulate in the OHP under the influence of electrostatic attraction.[83]

In order to reach industrial-level current density, the working potential has to be set below PZC, which leads to the accumulation of adsorbed AMCs at the electrode surface, causing the cation effects.[84,85] Specifically, the cation effects alter the hydrogen bond network connectivity, affect proton transfer, enhance the interface electric field strength, and influence the stability of reaction intermediates, which is directly related to the $2e^-$ ORR performance. Therefore, optimizing the electrode interface microenvironment is essential to enhancing the H_2O_2 electrosynthesis performance.

3.2.1 Adjusting protons at the reaction interface. It is observed that the FE of carbon electrodes tend to decline as the reaction overpotential increases, which is attributed to the side reaction of the H_2O_2RR.[86] Maintaining high H_2O_2 selectivity across a wide potential window is central to large-scale H_2O_2 production. Modulating the reactant proton by reducing both proton concentration and transfer rate will inhibit the H_2O_2RR. Besides, carbon electrodes typically exhibit good $2e^-$ ORR activity in alkaline electrolytes, but their activity diminishes under neutral and acidic conditions.[6] Reducing the proton concentration at the electrode interface could create an alkaline-like microenvironment, which enhances the 2e$^-$ ORR activity, and expands the applications of carbon electrodes to broader scenarios.

Adjusting protons using AMCs. AMCs can be used to modify the proton concentration at an electrode interface.[87,88] By adding trace amounts of Na^+ into H_2SO_4 electrolyte, it was found that under industry-relevant current values, negatively charged carbon electrodes could accumulate protons and Na^+ at the electrode interface by electrostatic interaction. Molecular dynamics simulations revealed that Na^+ was more competitive in occupying the double layer at the electrode interface, effectively repelling protons. This shielding effect of Na^+ on protons significantly reduced the proton concentration at the electrode interface, creating an alkaline-like microenvironment that improved H_2O_2 electrosynthesis, and this effect continued as the Na^+ concentration increased. By adding 0.1 M Na^+, the overpotential of the carbon electrode decreased by 0.6 V at 400 mA cm^{-2}, and the selectivity increased by nearly 80% (Fig. 6a).[86]

AMCs can also modify the proton transfer rate to the electrode interface. Recently, Cao *et al.*[89] investigated the cation effect on proton transfer rate by adding K^+ into the H_2SO_4 electrolyte. The solvated K^+ in the OHP reduced the connectivity of the hydrogen-bonds (H-bonds) network near the electrode surface, and inhibited the transfer of H_3O^+ to the electrode interface. Molecular dynamics simulations revealed that K^+ promoted H_2O dissociation at the electrode interface, facilitating the protonation of $*O_2$ or *OOH. Additionally, solvated K^+ and nearby H_2O could interact with the *OOH intermediate at the electrode interface, and enhance its stability (Fig. 6b).

Adjusting protons using organic additives. Cationic surfactants such as dodecyl tricaprylmethylammonium chloride (Aliquat 336), tetrabutylammonium bromide (TBAB), trimethylammonium bromide (DTAB), and cetyltrimethylammonium bromide (CTAB) can also adsorb on the electrode surface by electrostatic interaction as AMCs, and their unique chemical structures can introduce more possibilities. Gyenge *et al.*[92] found that electrostatically adsorbed Aliquat A336 molecules were able to replace protons on the carbon electrode surface, reducing the proton concentration at the electrode interface. The pH value at the carbon electrode interface was estimated to increase from 0.9 to 9.4 in 0.1 M H_2SO_4 electrolyte, which improved the 2e$^-$ ORR performance of the carbon electrode. TBAB was also found to enhance H_2O_2 production on carbon electrodes through a similar mechanism.[93]

As water molecules serve as the proton donor for the 2e$^-$ ORR in alkaline electrolytes, and the H-bonds network at the electrode interface dominates proton transfer rate to the interface,[94] controlling the number or altering the structure of H-bond

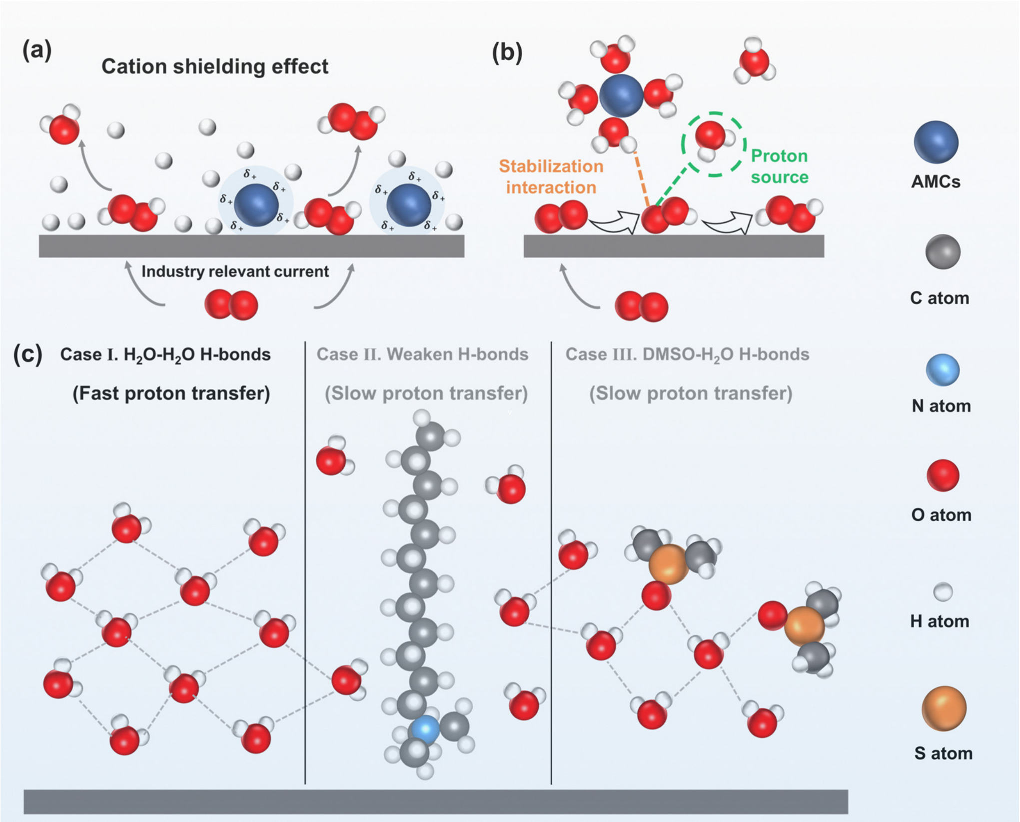

Fig. 6 (a) Schematic of the 2e$^-$ ORR in acid with/without AMCs under an industry-relevant current, reproduced with permission from ref. 86 copyright 2022, Springer Nature; (b) schematic of the solvated AMCs and adsorbed *OOH, reproduced with permission from ref. 89, copyright 2024, Wiley-VCH; (c) schematic of the interfacial H-bond network: H_2O–H_2O H-bonds enable fast proton transfer (case I), weakened H-bonds induced by DTAB (case II), and structurally altered H-bonds induced by DMSO (case III); both cases II and III resulted in slow proton transfer; adapted from ref. 90 and 91.

networks can regulate the proton transfer rate and inhibit the H_2O_2RR. Fan *et al.*[90] found that DTAB molecules adsorbed on the carbon electrode could repel water molecules away from the electrode interface. Therefore, the intensities of strong H-bonds in water and weak H-bonds in water at the electrode interface decreased from 3.02 to 0.69 and from 4.25 to 0.36 respectively, which weakened the strength of the H-bond network. Consequently, the proton transfer rate in the electrode interface was hindered, which inhibited the H_2O_2RR and enhanced H_2O_2 selectivity from 75% to 91% (case II in Fig. 6c).

However, the adsorption of cationic surfactants on the electrode may block the active sites and reduce electrode conductivity. Dimethyl sulfoxide (DMSO) is a strong hydrogen bond acceptor that can form robust H-bonds with water molecules, which was found to alter the original H-bond network structure.[95] Recently, Fang *et al.*[96] investigated the effect of DMSO on H_2O_2 electrosynthesis at carbon electrodes by altering the H-bond network. The result revealed that the DMSO formed stronger H-bonds with H_2O (DMSO–H_2O H-bonds) compared to H_2O–H_2O H-bonds. As DMSO could not supply protons, and the stronger H-bonds further inhibited water dissociation, this limited proton transfer to the electrode surface and in turn improved H_2O_2 selectivity from 60% to 90% (case III in Fig. 6c).

Adjusting protons by engineering carbon electrode microstructures. Although the addition of cationic surfactants and organic solvents to an electrolyte can modify proton at the electrode interface, it inevitably introduces impurities into the H_2O_2 solution. Designing the microstructure of carbon electrodes enables self-modification of protons at the electrode interface. For instance, Yang *et al.*[97] built an O_2-accumulation interface microenvironment by introducing a hydrophobic microporous layer into the GDE substrate, which promoted the proton-consuming rate and inhibited further protonation of H_2O_2, achieving approximately 100% H_2O_2 selectivity. Recent studies reported that precisely engineered carbon electrode structures, such as mesoporous hollow nanoreactors (MHNs),[98] mesoporous carbon nanosheets (MeCNs),[99] and micro/mesoporous N, O co-doped carbon nanosheets (N, O-CNS$_x$),[100] showed similar promoting effects by adjusting protons at the electrode interface and improved $2e^-$ ORR performances.

It is worth noting that although an alkaline-like microenvironment at the electrode interface improved $2e^-$ ORR performance, the negatively charged carbon electrode tends to repel OH^- from the electrode surface to bulk solution, offsetting the promoting effect of alkaline-like microenvironments.[101] Lewis acids were found to accept a pair of electrons from OH^-, forming new chemical bonds that could enhance OH^- adsorption.[102,103] Based on this, Li *et al.*[104] synthesized Lewis acid TiO_2 modified CB (CB–$x$$TiO_2$) catalysts using a thermal decomposition method; TiO_2 adsorbed *in situ* generated OH^- and established a stable alkaline-like microenvironment, which improved the H_2O_2 yield in neutral electrolyte (52.5 mmol L^{-1} h^{-1}) close to that in alkaline electrolyte (58.4 mmol L^{-1} h^{-1}).

3.2.2 Controlling the electric field at the reaction interface.

The electric field at the electrode–electrolyte interface plays a central role in driving the electrocatalytic reactions. Kelly *et al.*[105] developed a microkinetic model for the ORR, by incorporating the electric field effects into the established computational hydrogen electrode model, and demonstrated that the binding energies of key intermediates such as *OOH, $^*O_2$ and $^*H_2O_2$ increased with the enhancement of the interfacial electric field (Fig. 7a). This study established a correlation between the binding energies of ORR intermediates and the electric field strength, providing a solid theoretical foundation for future research in this area.

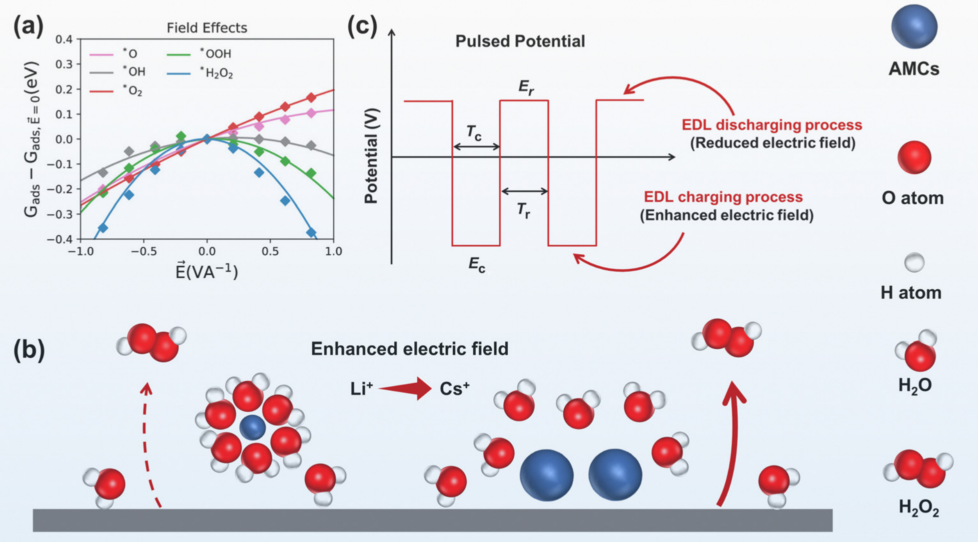

Fig. 7 (a) Influence of simulated interfacial electric fields on the adsorption energies of various intermediates during the ORR, reprinted with permission from ref. 105, copyright 2020, American Chemical Society; (b) AMC size effect on the electric field, the large radius AMC (Cs^+) enhanced electric field more pronouncedly than the small radius AMC (Li^+), adapted from ref. 106; (c) parameters in pulsed potential and their effects on electric field, adapted from ref. 107.

Addition of AMCs not only adjusts the proton at the electrode interface, as discussed in the previous section, but also modifies the electric field strength, which originates from the electrostatic interactions between the negatively charged carbon electrodes and AMCs.[108,109] Density functional theory calculations revealed that solvated K^+ in the double layer increased the interfacial electric field strength by 0.77–1.44 V $Å^{-1}$, and the AMC-induced interface electric field effect could shift ΔG_{*OOH} toward the top of the activity volcano plot.[85]

The AMC-induced interface electric field effect was also found to relate to the size of AMCs. A study showed that the enhancement was in the order of $Cs^+ > K^+ > Li^+$.[106] Li^+ with smaller radius and higher charge density, attracted more water molecules and formed a larger hydration layer. Instead, Cs^+ formed a smaller hydration layer due to its larger radius, making it easier to approach the electrode surface, which enhanced the interfacial electric field strength (Fig. 7b). Increasing the concentration of AMCs could further enhance the interfacial electric field strength, thus improving H_2O_2 electrosynthesis performance.

Similarly, adding cationic surfactants to the electrolyte can also modify the interfacial electric field strength through electrostatic effects. Chen *et al.*[110] hypothesized that the adsorption of CTAB could reduce the distance between the OHP and IHP in the double layer, which enhanced the electric field strength at the electrode interface, and in turn optimized the binding energy of the *OOH intermediate. Consequently, the ORR activity increased by three-fold, and the H_2O_2 selectivity improved from 60% to 93%. The electric field strength at the electrode interface could also be modified by preparing electrodes with specific morphologies.[111] For example, by using an Au needle electrode, the electric field strength increased by ten-fold, resulting in significantly improved CO_2RR performance.[112] This tip-induced electric field strength effect could be applied in the H_2O_2 electrosynthesis, however, to the best of our knowledge, no relevant research has been conducted in the field of the $2e^-$ ORR.

Electrochemical techniques, such as pulse voltammetry, have been used to directly modify the strength of the electric field at the electrode interface, as shown in Fig. 7c. Key parameters include the cathodic pulsed potential (E_c), cathodic pulsed duration (T_c), rest potential (E_r) and rest duration (T_r). Different from the constant potential electrocatalysis, pulse electrocatalysis involves repetitive charging and discharging of the electrode and modifies the electric field periodically. Ding *et al.*[107,113] demonstrated that the pulse electrocatalysis method could modify the adsorption of *OOH intermediates by affecting the interface electric field strength. The discharging of the EDL at rest potential resulted in a reduced electric field strength at the electrode interface, decreasing the adsorption strength of the *OOH intermediate, which consequently increased the H_2O_2 yield by 138%.

4 Reactors for H_2O_2 electrosynthesis

Managing the surface wettability and modifying the interface microenvironment of carbon electrodes play critical roles in improving the $2e^-$ ORR performance. Moreover, the design of reactor configurations directly influences the practical performance of H_2O_2 electrosynthesis. In this section, the design of the reactor key components will be further reviewed; the challenges and mitigation measures in real-world electrosynthesis will also be discussed.

4.1 Reactor design

4.1.1 Key components in a reactor. A flow-cell reactor typically consists of two flow field plates (FFP), two electrolyte compartments (EC), a cathode, an anode, and an ion exchange membrane (IEM), as shown in Fig. 8a. Although numerous catalysts have been developed for the $2e^-$ ORR, their performance evaluations were limited to laboratory-scale devices such as RRDE and H-cell,[64,114,115] and only few studies have focused on the optimization of GDE reactors to evaluate the practical performance of H_2O_2 electrosynthesis.[116,117] The design of reactor key components has a significant impact on electrocatalytic performance. For example, high ohmic resistance and low gas diffusion efficiency within the reactors can hinder effective H_2O_2 production, which necessitates the optimization of reactor systems.

The flow field plate (FFP) is a crucial component of the reactor, which supports the reactor structure, conducts electrons, and transports gaseous reactants.[24] The geometric design of gas flow channels in the FFP includes a straight parallel channel, serpentine channel, and interdigitated channel.[119] A well-designed gas flow channel can effectively regulate the flow rate of O_2 to the electrode, ensuring uniform distribution across the electrode surface and reducing pressure loss,[120] which subsequently improves the O_2 diffusion efficiency and H_2O_2 production.

Current studies have generally utilized a serpentine flow channel and interdigitated channel for H_2O_2 electrosynthesis,[30,121] as illustrated in Fig. 8b. The serpentine flow channel (left in Fig. 8b) allows O_2 to flow from the inlet to the outlet along the path, resulting in the parallel diffusion of O_2 to GDE. Nevertheless, a significant loss of gas pressure will be observed in a long serpentine channel, which will reduce the O_2 supply near the outlet of the channel and lead to electrode flooding.[122] In the interdigitated channel (on the right in Fig. 8b) the O_2 at the inlet initially diffuses parallelly to the GDE and is then forced to diffuse vertically into the electrode, which effectively enhances the mass transfer of O_2 to the GDE.[31] Electrocatalytic performance comparison between the serpentine and interdigitated flow channels showed that the current densities of H_2O_2 in both channels increased linearly with the rising overpotential at a current density below 100 mA cm^{-2}. Moreover, the current density in the interdigitated channel kept increasing at a current density above 100 mA cm^{-2}, while it decreased in the serpentine channel due to the insufficient O_2 diffusion induced electrode flooding (Fig. 8c).[30]

Materials with high mechanical strength, excellent electrical conductivity, and high durability to corrosion are required for FFP fabrication in H_2O_2 electrosynthesis. Stainless steel is commonly applied in FFP fabrication due to its high mechanical strength and conductivity, but its durability is unsatisfactory as the generated H_2O_2 accelerates the corrosion and oxidation of metallic steel, forming metal oxide films that increase the contact

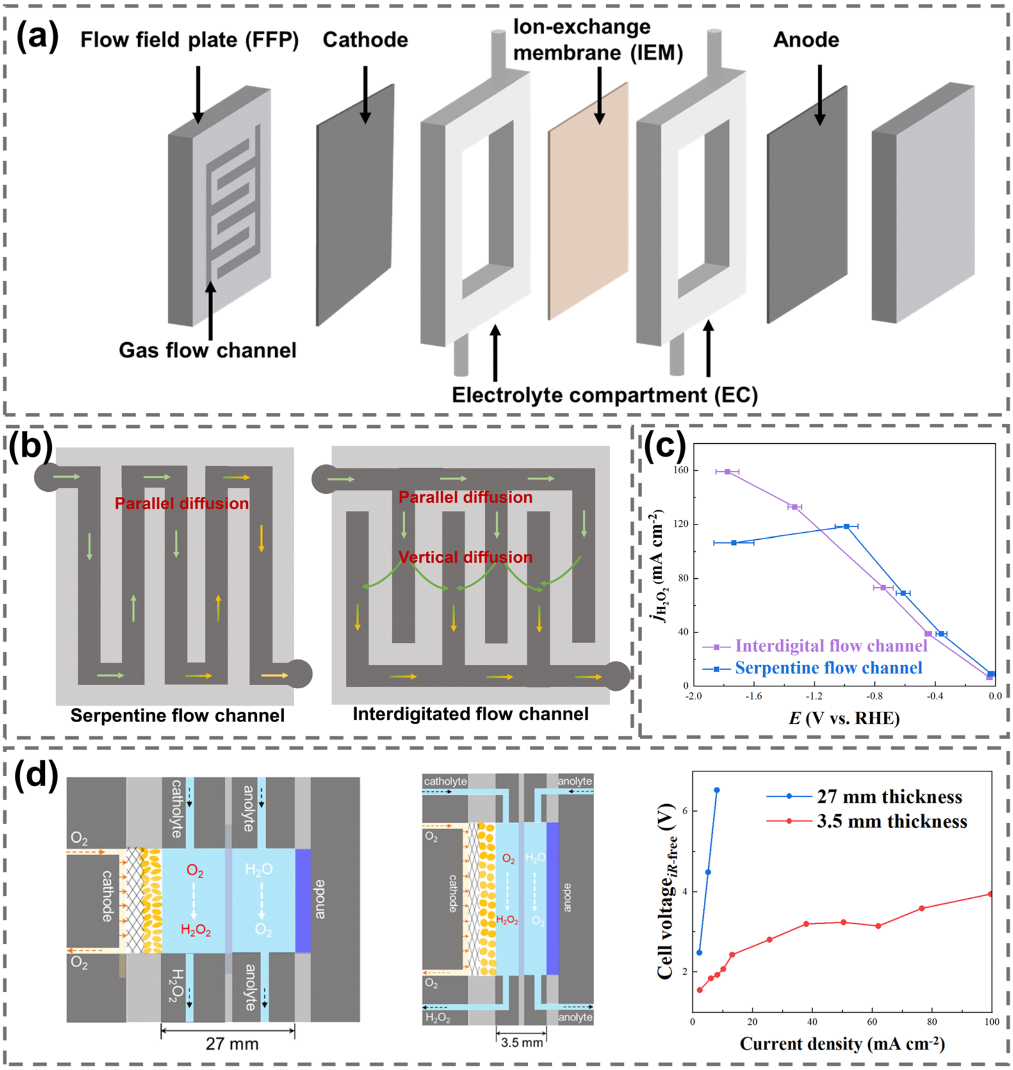

Fig. 8 (a) Key components in a typical flow-cell reactor; (b) schematic of the FFPs with a serpentine flow channel (left) and interdigitated flow channel (right), reproduced with permission from ref. 31, copyright 2021, Springer Nature; (c) H_2O_2 current densities using a serpentine flow channel and interdigitated flow channel; data were taken from ref. 30; (d) schematic of H_2O_2 electrosynthesis using two reactors with different EC thicknesses (27 mm and 3.5 mm), and their H_2O_2 electrosynthesis performance, reprinted with permission from ref. 118, copyright 2023, Springer Nature.

resistance between the FFP and GDE.[24] Compared to metallic materials, graphite sheets offer high durability for H_2O_2 electrosynthesis while maintaining high conductivity, but suffer from low mechanical strength and potential gas permeability issues. Developing graphite-based composite materials may address those issues to achieve high strength, conductivity, and durability.

The design of electrolyte compartment (EC) has a significant impact on the internal resistance of the reactor.[123] To prevent H_2O_2 from reacting with EC materials, corrosion-resistant and high-strength plastics materials such as polyether ether ketone (PEEK) and polytetrafluoroethylene (PTFE) are commonly utilized. The thickness of EC directly affects the overall internal resistance of the reactor. By decreasing the EC thickness from 27 mm to 3.5 mm, the internal resistance of the reactor was reduced and the overall electrocatalytic performance was improved, with the cell voltage dropping from 6 V to 2 V at 10 mA cm^{-2}, as shown in Fig. 8d.[118] Notably, the addition of solid electrolyte (SE) in the EC could also effectively lower the internal resistance in reactors.[124] Styrene-divinylbenzene copolymer microspheres, Dowex 1 × 8 anion conductor resins, and inorganic $Cs_xH_{3-x}PW_{12}O_{40}$ proton conductors were often employed as the SE materials due to their high ion conductivity.[22,117,125–127]

It has to be pointed out that the evaluations of H_2O_2 electrocatalysts in the laboratories are typically performed with laboratory-scale three-electrode system GDE reactors, focusing on the half-cell reaction rather than the overall reaction performance. The internal resistance of the three-electrode system is directly related to the distance between the reference and working electrodes, rather than the EC thickness. Moreover, laboratory-scale GDE reactors possess a small working electrode area (1 cm^{-2}) with short FFP channels, which could facilitate O_2 diffusion. Therefore, in our opinion, the design of the FFP and EC has minimal improvement for H_2O_2 electrocatalytic in laboratory-scale GDE reactors, but it is very important to optimize those reactor components for industry-level H_2O_2 production.

4.1.2 Reactors for H_2O_2 electrosynthesis *via* an energy-consuming mode. The electrochemical synthesis of H_2O_2 *via* the $2e^-$ ORR can be classified into two modes based on the anodic reaction, as shown in Fig. 9a. When the working potential of the anodic reaction is higher than 0.7 V, typically for the ethylene glycol oxidation reaction (EOR), oxygen evolution reaction (OER) and $2e^-$ water oxidation reaction ($2e^-$ WOR), the reactor can only operate in an energy-consuming mode to produce H_2O_2. In contrast, when the working potential of the anodic reaction is lower than 0.7 V (*e.g.* the hydrogen oxidation reaction, HOR), the reactor can operate in an energy-producing mode, enabling the co-generation of both H_2O_2 and electricity. The performances of various GDE-based reactors are summarized in Table S1 (ESI†).

In 1939, Berl proposed H_2O_2 electrosynthesis using activated carbon electrode as the cathode, which produced high concentrations of H_2O_2 and was anticipated to be commercially utilized.[132] Initially, the commercial production of H_2O_2 through electrosynthesis relied on the Huron Dow process (on the left in Fig. 9b).[128] This process used a strong alkaline solution as the electrolyte, wherein O_2 was introduced into the electrolyte and reduced to HO_2^- at the cathode. The efficiency of this process was constrained by the low solubility of O_2 in the electrolyte (∼9 ppm at 25 °C),[133] as well as the inevitable decomposition of H_2O_2 in a strong alkaline solution.

The flow-cell using GDE as the cathode could significantly enhance the O_2 mass transfer, and in turn increase the production rate of H_2O_2 (in the middle in Fig. 9b). However, the cation exchange membrane (CEM) used for separation would be gradually degraded by H_2O_2,[134] which presented a great challenge to the long-term stability. A membrane-free reactor was then proposed by Chen *et al.*[129] which could eliminate this issue ultimately. The reactor consisted of two carbon paper electrodes with the sides facing the catholyte coated with a hydrophobic polymer, which allowed the diffusion of gaseous O_2 but prevented H_2O_2 from crossing to the anode (on the right in Fig. 9b). In addition, the membrane-free reactor exhibited improved H_2O_2 electrosynthesis due to the reduced internal resistance by removing the CEM.

The cathodic $2e^-$ ORR is typically coupled with the anodic OER, which is kinetically sluggish and generates low-value O_2.[135] Replacing the OER with thermodynamically favorable

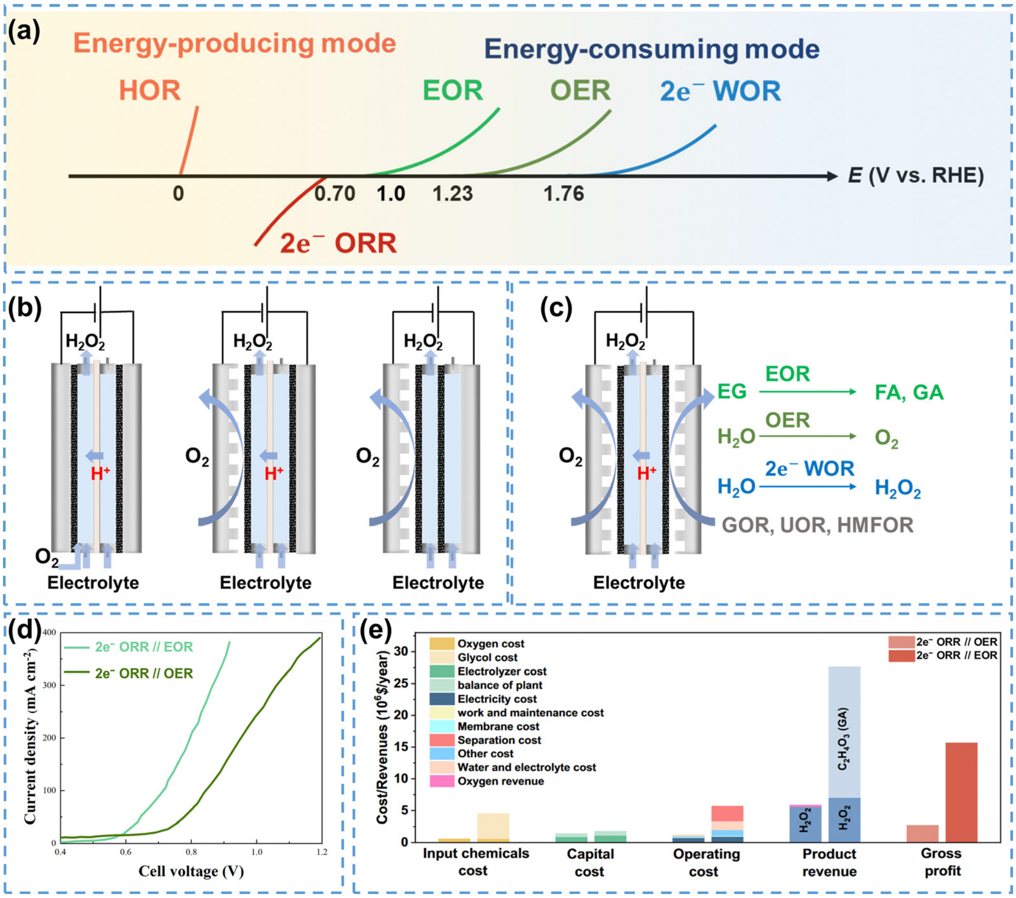

Fig. 9 (a) Coupled systems of the $2e^-$ ORR and possible anodic reactions; (b) the Huron–Dow process (left), adapted from ref. 128; conventional GDE flow-cell reactor (middle); membrane-free flow-cell reactor (right), adapted from ref. 129; (c) schematic of coupled systems for $2e^-$ ORR production and high-value chemicals synthesis; (d) performance comparison of the $2e^-$ ORR//EOR and $2e^-$ ORR//OER systems, data were taken from ref. 130; (e) technoeconomic evaluation of the $2e^-$ ORR//OER and $2e^-$ ORR//EOR systems, reprinted with permission from ref. 131, copyright 2024, Springer Nature.

organic oxidation reactions can improve the overall energy efficiency and economic viability of the system. Organic oxidation reactions such as the ethylene glycol oxidation reaction (EOR),[130] glycerol oxidation reaction (GOR),[136] urea oxidation reaction (UOR),[137] 5-hydroxymethylfurfural oxidation reaction (HMFOR),[138] and furfural oxidation reaction (FuOR)[139] have been used as the anodic reaction to couple with the $2e^-$ ORR, as shown in Fig. 9c. Taking EOR as an example, the onset potential for the EOR is below 1 V, which is much lower than that required for the OER. In addition, ethylene glycol can be converted into value-added formic acid (FA) and glycolic acid (GA) through electrocatalytic reactions. As shown in Fig. 9d, the $2e^-$ ORR//EOR coupled system required only 0.9 V to achieve an industrial level current density of 400 mA cm^{-2}, while the $2e^-$ ORR//OER system required a higher voltage of 1.2 V, which demonstrated the superior efficiency of the EOR-based system.[130] Similarly, Sun *et al.*[131] employed EOR as the anodic reaction and selectively oxidized ethylene glycol to high-value GA, which significantly increased the gross profit of the coupled system (Fig. 9e).

Theoretically, replacing the OER with the $2e^-$ WOR could increase the H_2O_2 FE up to 200%, thus improving both the H_2O_2 production rate and the energy utilization efficiency.[140,141] Xia *et al.*[142] constructed the $2e^-$ ORR//$2e^-$ WOR coupled system with oxygen-functionalized carbon nanotubes (O-CNTs) as the cathode and PTFE-coated carbon fiber paper (CFP-60%) as the anode, which enabled the simultaneous electrochemical synthesis of H_2O_2. This coupled system achieved an H_2O_2 FE exceeding 150% at 120 mA cm^{-2}, highlighting the significant potential of carbon electrodes for the efficient production of H_2O_2 *via* $2e^-$ ORR and $2e^-$ WOR processes.

4.1.3 Reactors for H_2O_2 electrosynthesis *via* the energy-producing mode. H_2O_2 can also be produced in an energy-producing mode, which is also referred to as the H_2–O_2 fuel cell method, with a theoretical maximum output voltage of ~0.7 V. In the 1990s, Yamanaka *et al.*[143] first introduced the concept of H_2O_2 electrosynthesis using proton exchange membrane fuel cells (PEMFCs), and they further developed PEMFCs for neutral H_2O_2 solution generation.[144,145] Afterwards, Li *et al.*[146] achieved the continuous synthesis of neutral H_2O_2 by PEMFCs over 72 hours with an H_2O_2 yield of 200 μmol h^{-1} cm^{-2} and a 30% current efficiency, which showed promising application for residential drinking water disinfection. As illustrated in Fig. 10a, the PEMFC consisted of two FFPs and a membrane electrode assembly (MEA), wherein protons are generated by the HOR and transferred to the cathode through the CEM, which further combine with O_2 to form H_2O_2. The MEA is prepared by hot-pressing the sandwich structure of the cathode, CEM, and anode, forming a zero-gap structure with negligible internal resistance.

The integrated PEMFC stack reactor is beneficial for large-scale H_2O_2 electrosynthesis. Nevertheless, the zero-gap structure of the MEA hinders the transportation and collection of produced H_2O_2, resulting in a high concentration of H_2O_2 within the MEA, which accelerates the H_2O_2RR and reduces the H_2O_2 selectivity. Various optimization strategies were adopted to mitigate this issue, including catalyst loading adjustment, MEA wettability modification, flow rate controlling, and reaction temperature regulation.[149] Besides, the preparation methods of the MEA, including catalyst-coated membranes (CCM) and gas diffusion electrodes also influence the PEMFC performance for H_2O_2 electrosynthesis.[150]

In recent years, alkaline anion exchange membrane fuel cells (AEMFCs), which operate under milder conditions compared to PEMFCs, have garnered increasing attention. Carbon electrodes are well known for their excellent $2e^-$ ORR performance under alkaline conditions, thus exhibiting great potential in AEMFC for H_2O_2 electrosynthesis.[6] Unlike PEMFCs that produce H_2O_2 at the cathode, AMEFCs produce HO_2^- ions at the cathode, which pass through an anion exchange membrane (AEM) to the anode, and further combine with protons to form H_2O_2 (Fig. 10b). In addition to the H_2O_2 transfer hindrance in the MEA, another challenge arises in AEMFCs due to the strong decomposition ability of anodic catalysts towards H_2O_2, such as Pt/C, which inhibits the production of H_2O_2. The low ionic conductivity of AEM presents an additional challenge to the AEMFC performance,[151] requiring more efforts to enhance the conductivity of AEM for better H_2O_2 electrosynthesis performance.

Using a solid electrolyte (SE) layer instead of conventional ion exchange membranes can effectively address the aforementioned issue of H_2O_2 transport in MEA, facilitating the co-generation of H_2O_2 and electricity. As illustrated in Fig. 10c, Xia *et al.*[147] proposed a dual membrane solid–electrolyte cell consisting of AEM, CEM, and SE layers in between, which was composed of sulfonated styrene-divinylbenzene copolymer microspheres. In the reactor, H^+ generated at the anode were conducted through the CEM and the HO_2^- generated at the cathode were conducted through the AEM, and they further combined to form H_2O_2 within the SE layer, ensuring high concentration H_2O_2 production (up to 20 wt%). Rawah *et al.*[63] optimized the dual membrane reactor by removing the AEM and applying a hydrophobic treatment to the carbon electrode, which reduced the reactor internal resistance and enhanced the electrocatalytic performance (Fig. 10d). Following the same concept, the combination of anionic solid electrolyte and AEM could theoretically generate H_2O_2 in energy-producing mode, as depicted in Fig. 10e.

Apart from H_2–O_2 fuel cells, metal–air batteries such as zinc–air batteries (ZABs) are promising for H_2O_2 electrosynthesis under energy-producing mode. As shown in Fig. 10f, the typical structure of a ZAB consists of a zinc plate (for the oxidation reaction) and an air electrode (as the cathode for the $2e^-$ ORR). Wang *et al.*[148] first demonstrated the feasibility of H_2O_2 production using ZAB by employing a carbon electrode as the air electrode, achieving an output power of 36 mW cm^{-2} with a H_2O_2 yield of 0.593 mmol cm^{-2} h^{-1} at 0.8 V. Furthermore, Xie *et al.*[152] improved the ZAB performance by using S-doped carbon as the air electrode, which increased the maximum output power to 82.7 mW cm^{-2} and maintained a high H_2O_2 production rate. Since H_2O_2 is unstable in strong alkaline electrolytes, which are commonly used in ZABs (6 M KOH), Lu *et al.*[153] developed a neutral ZAB to avoid the decomposition of H_2O_2, which exhibited a high H_2O_2 selectivity of 91% and maintained a long-time stability up to 1500 hours in a low-temperature environment.

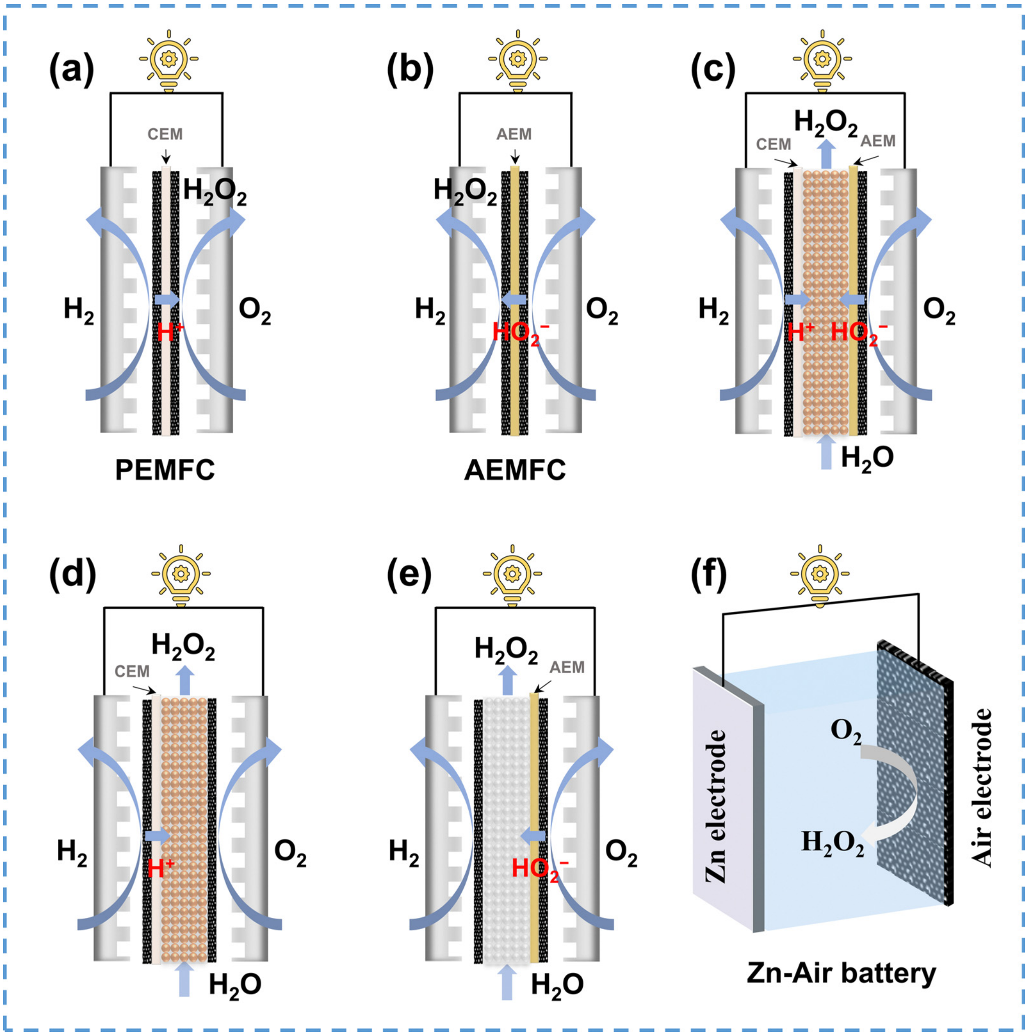

Fig. 10 Schematic of various reactor configurations for H_2O_2 electrosynthesis in energy-producing mode: (a) proton exchange membrane fuel cell (PEMFC), adapted from ref. 143; (b) alkaline anion exchange membrane fuel cell (AEMFC), (c) dual membrane solid–electrolyte cell (SE-cell), adapted from ref. 147; (d) CEM solid–electrolyte cell, adapted from ref. 63; (e) AEM solid–electrolyte cell, and (f) Zn–air battery, adapted from ref. 148.

4.2 Considerations in practical-scale H_2O_2 electrosynthesis

4.2.1 Evolution of catalysts under *operando* conditions. One of the main challenges for continuous practical-scale H_2O_2 electrosynthesis is that the catalysts must be able to resist the harsh oxidative electrolytic conditions. Hitherto, various catalysts have been developed and used for the laboratory scale production of H_2O_2 in GDE reactors (Tables S2 and S3, ESI†), such as sulfides and selenides,[154,155] transition metal alloys,[156,157] and single-atom catalysts,[158,159] yet, the possible dynamic evolution and *in situ* reconstruction of catalyst materials under *operando* conditions have often been overlooked. In this section, we focus on the evolution of catalysts under *operando* conditions instead of catalyst design, and readers who are interested in catalyst design are referred to the latest reviews.[156–162]

Catalysts in a strongly oxidizing H_2O_2 environment could undergo dynamic evolutions, as the produced H_2O_2 may react with the catalysts, especially metal oxides,[163,164] leading to changes in the electrochemical properties of the catalysts. For example, ZnO has been recognized as a promising catalyst for H_2O_2 production,[165–167] however, this material could be converted to ZnO_2 by H_2O_2,[168] which inspires further investigations on the true active sites of ZnO electrocatalysts. Recently, Zhou *et al.*[163] observed that using ZnO as the $2e^-$ ORR catalyst, the H_2O_2 selectivity increased from 64.45% to nearly 100% within 6000 s (Fig. 11a). Raman spectroscopic studies of the ZnO pristine catalyst, activated at 0.2 V in O_2-saturated electrolyte for different reaction times, confirmed the appearance of O_2^{2-} signal (Fig. 11b), suggesting the *in situ* construction of a ZnO@ZnO_2 heterogeneous structure. Density functional theory (DFT) calculations indicated that the heterogeneous interface between ZnO and the *in situ* constructed ZnO_2 was likely the real active sites, which weakened the binding energies of both *OOH and *O_2 and facilitated superior $2e^-$ ORR performance (Fig. 11c). This hypothesis was further supported by the fact that ZnO@ZnO_2 synthesized using 0.1 M H_2O_2 exhibited nearly identical selectivity as the ZnO@ZnO_2 heterostructure evolved from ZnO under *operando* conditions. Similarly, using Ti_2O_3 as the initial $2e^-$ ORR catalyst, the surface of Ti_2O_3 could

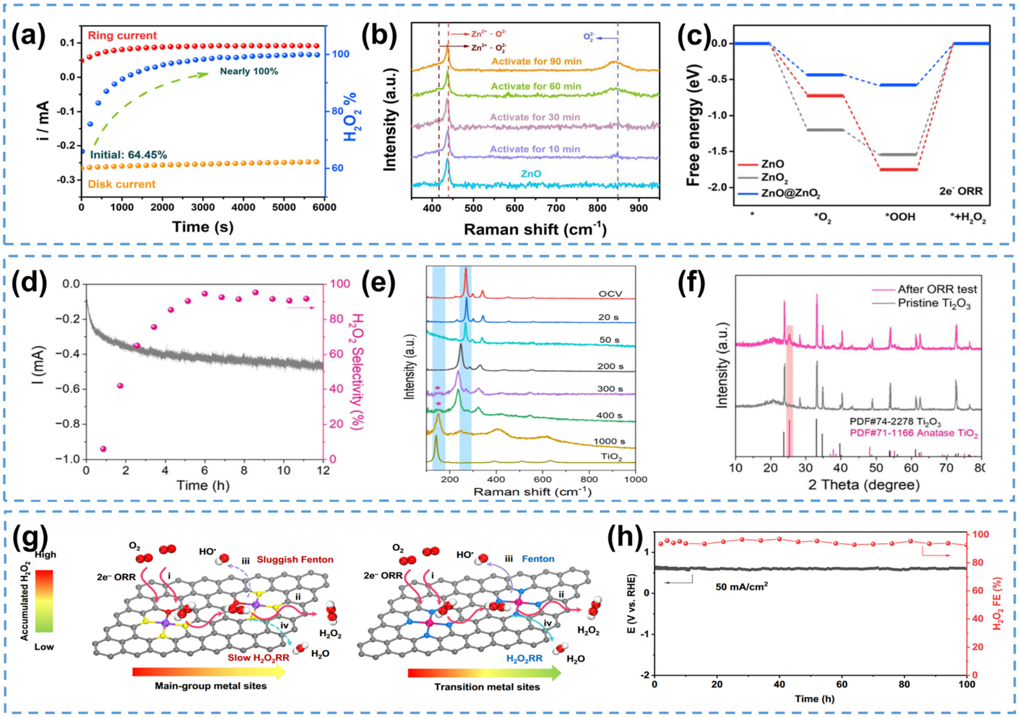

Fig. 11 (a) Chronoamperometry measurement of the $2e^-$ ORR on ZnO at 0.2 V, and H_2O_2 selectivity, (b) Raman spectra of ZnO electrochemically activated at 0.2 V for different periods of time, and (c) energy diagram of $2e^-$ ORR intermediates on ZnO, ZnO_2 and ZnO@ZnO_2 (U = 0.7 V); (a)–(c) are reprinted with permission from ref. 163, copyright 2023, Royal Society of Chemistry; (d) chronoamperometry measurement of the $2e^-$ ORR on Ti_2O_3 at 0.3 V and H_2O_2 selectivity, (e) *in situ* Raman spectra collected during the $2e^-$ ORR on Ti_2O_3 at 0.2 V, and (f) XRD spectra of Ti_2O_3 before and after ORR electrocatalysis; (d) and (e) are reprinted with permission from ref. 164, copyright 2023, Royal Society of Chemistry; (g) schematics of Fenton reaction rate on the main-group metal catalysts (left) and transition metal catalysts (right), and (h) chronopotentiometry measurement on Pb SA/OSA at 50 mA cm^{-2}, and H_2O_2 selectivity; (g) and (h) are reprinted with permission from ref. 169, copyright 2024, Springer Nature.

transform into oxygen-deficient TiO_2 during the reaction, which switched the ORR pathway from the $4e^-$ to $2e^-$ pathway (Fig. 11d), and this surface reconstruction from pristine Ti_2O_3 to TiO_2 was subsequently confirmed by *in situ* Raman spectroscopy study (Fig. 11e) and XRD spectra collected after the ORR test (Fig. 11f).[164]

The electrochemically generated H_2O_2 could also potentially induce the Fenton-like reactions, especially on transition metal catalysts,[170] which produces strong oxidative ROS, raising concerns on the catalyst durability. Different from transition metals, main-group metals are Fenton-inactive for their fully occupied d-orbitals, and thus considered as an attractive option for mitigating Fenton-like reactions. Recently, Zhou *et al.*[169] reported the main-group Pb SACs (Pb SA/OSC) catalyst for H_2O_2 electrosynthesis, achieving an industrial current density of 400 mA cm^{-2} with remarkable FE (∼90%). No ROS characteristic signals were observed during the $2e^-$ ORR process, suggesting that Pb SACs had sluggish Fenton reaction rate compared to transition metal catalysts (Fig. 11g). This catalyst also exhibited excellent durability without degradation at 50 mA cm^{-2} (FE maintained over 90%) for at least 100 hours (Fig. 11h). It is also found that adding a radical scavenger (typically CeO_2) could protect the catalyst from being attacked by radicals and improve the durability of ORR catalysts in PEMFC applications.[171,172] This strategy could be potentially applied in $2e^-$ ORR electrocatalyst design to rapidly eliminate ROS and improve the catalyst durability.

4.2.2 Operational challenges and mitigation measures.

Although many efforts have been made in catalyst development, electrode modification, and reactor design, many challenges of H_2O_2 electrosynthesis under practical-scale operation have not been fully addressed. This section focuses on the issues during the operation of the device, such as the Joule heating effect, electrode fouling issue, and membrane degradation; the corresponding mitigation measures will also be discussed.

Joule heating is a universal phenomenon in electrolysis processes, which originates from the internal ohmic resistance in devices (eqn (15)).

$$Q = i^2Rt \tag{15}$$

where Q, i, R, and t are the generated heat (J), applied cell current (A), ohmic resistance (Ω) and reaction time (s) respectively.

During electrolysis processes, Joule heating is mainly manifested by an increase in electrolyte temperature, severely affecting the H_2O_2 selectivity by promoting its self-decomposition reaction rate, especially in an alkaline environment under industrial current density.[32] Recently, Ni *et al.*[173] investigated

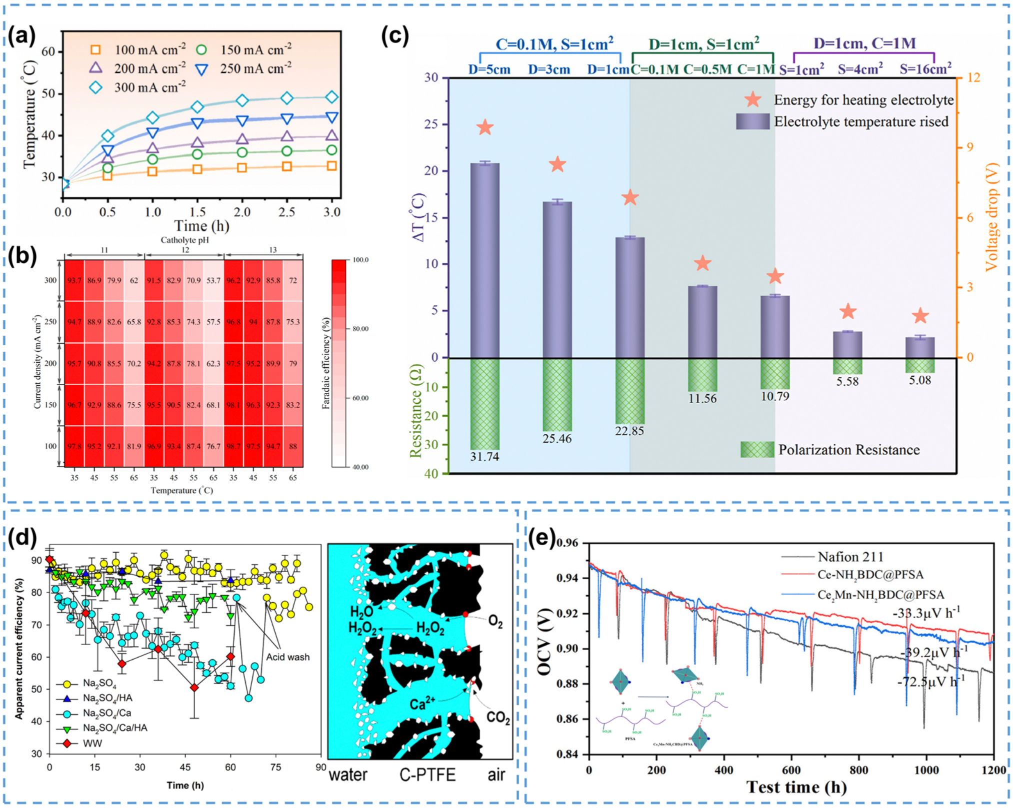

Fig. 12 (a) Temperature of the electrolyte during the reaction at different current densities, (b) calculated H_2O_2 FE under different current densities and temperatures, (c) cell voltage drop, electrolyte temperature change, and cell resistance under different cell configurations; (a) and (b) are reprinted with permission from ref. 173, copyright 2024, American Chemical Society, and (c) is reprinted with permission from ref. 32, copyright 2024, Elsevier Ltd; (d) apparent current efficiency of H_2O_2 production in different natural waters (left), and schematic of $CaCO_3$ precipitation process during H_2O_2 electrosynthesis (right), reprinted with permission from ref. 33, copyright 2023, Elsevier Ltd; (e) OCV holding test of $Ce_2Mn\text{-}NH_2BDC@PFSA$, $CeNH_2BDC@PFSA$, and Nafion 211 membranes, and schematic of the MOF and PFSA composite membrane (inset), reprinted with permission from ref. 174, copyright 2024, American Chemical Society.

the effect of current density on Joule heating by measuring the temperature of the electrolyte during electrolysis, and found that the temperature of the electrolyte gradually rose from 32.7 °C to 49.3 °C with increasing current density from 100 mA cm^{-2} to 300 mA cm^{-2} (Fig. 12a). Calculations showed that the H_2O_2 FE negatively correlated with the electrolyte temperature, consistent with experimental observations, indicating the promoting effect of Joule heating on H_2O_2 self-decomposition (Fig. 12b).

The Joule heating effect not only reduces the H_2O_2 FE, but also brings additional energy loss of the entire reactor. The cell resistance is regarded as a determining factor in the Joule heating effect, and the mitigation measures include reducing the electrolyte compartment thickness and increasing electrolyte conductivity *etc.*, which have been reviewed in Section 4.1.1. Researchers validated the effectiveness of these measures by reducing the electrode distance from 5 cm to 1 cm, increasing the electrolyte concentration from 0.1 M to 1 M, and expanding the electrode area from 1 cm^2 to 16 cm^2. Correspondingly, the cell resistance declined from 31.74 Ω to 5.08 Ω, and the temperature change (Δt) dropped from 20.9 °C to 2.2 °C, indicating a suppressed Joule heating effect (Fig. 12c).[32] Considering that the scale-up of H_2O_2 electrosynthesis to industrial current density level would inevitably magnify the Joule heating effect, heat management becomes indispensable. Integrating the reactor with a cooling system may be an effective solution in terms of suppressing the Joule heating effect.

For household disinfection and/or waste water treatment, it is desirable to directly use tap water or natural water due to their accessibility, instead of the de-ionized water used in laboratories, in order to reduce the overall processing cost. However, the existing hardeners (such as Ca^{2+}, Mg^{2+}) and other dissolved organic matter in natural water usually cause fouling issues on electrodes during the electrocatalysis process, resulting in decreased electrode stability and selectivity. For example, Ma *et al.*[33] found that the addition of Ca^{2+} in Na_2SO_4 solution led to a continuous decrease in the apparent current efficiency of H_2O_2 on carbon-based air diffusion electrodes (on the left in Fig. 12d). The $CaCO_3$ precipitates negatively influenced the electrode by covering the active sites, and more severely, the hydrophilic $CaCO_3$ precipitates could induce electrode flooding, resulting in sluggish mass transfer of O_2 (on the right in Fig. 12d). The fouling issue caused by Ca^{2+}/Mg^{2+} could be relieved by using complexing agents, which bond with Ca^{2+}/Mg^{2+}, significantly reducing their precipitation on the electrode surface.[175]

As one of the limiting factors for the long-term operation of H_2O_2 reactors, the stability of ion exchange membranes presents another challenge for the industrial production of H_2O_2. Currently, perfluorinated sulfonic acid (PFSA) based membranes (such as Nafion membranes) are commonly used for H_2O_2 electrosynthesis, however, they are prone to chemical degradation, which could be accelerated by various ROS species.[176–179] Recently, novel stable membranes such as sulfonated polyphenylene membranes,[180] hydrocarbon-based membranes,[181] and sulfonated fluorene-based poly(phenyl ketone) membranes[182] have been developed. Huang *et al.*[174] utilized a self-assembly method to synthesize a molecular organic framework (MOF)-PFSA composite membrane (Fig. 12e inset), in which the MOF material (Ce_2Mn-NH_2BDC) could efficiently scavenge free radicals and mitigate the membrane degradation issue in PEMFCs. The open circuit voltage (OCV) decay rate of this composite membrane was 33.3 μV h^{-1} within a 1200-hour test, much smaller than 72.5 μV h^{-1} for the commercial Nafion 211 membrane, which indicated its excellent chemical stability (Fig. 12e). These novel ion exchange membranes have the potential to be applied in H_2O_2 electrosynthesis reactors. Recently, preliminary attempts have been made to develop membrane-free reactors in order to reduce the internal ohmic resistance and overall cost,[129] which in fact could ultimately eliminate the membrane degradation issue.

5 $2e^-$ ORR integrated tandem systems for chemical synthesis

H_2O_2 is an important green oxidant and raw chemical material, with more than 30% of commercial H_2O_2 being used in traditional chemical synthesis.[6] For example, H_2O_2 is widely used for the epoxidation of alkene,[1] with titanium silicalite-1 (TS-1) serving as a highly active and selective catalyst when H_2O_2 is the primary oxidant.[183] For the decarbonization of the traditional chemical manufacturing industry, integrating electrochemically produced H_2O_2 into chemical synthesis represents an innovative approach to the synthesis of high-value chemicals.[184] In this section, we reviewed recent studies on the chemical synthesis using *in situ* generated H_2O_2.

5.1 Ex-cell and in-cell modes of tandem systems

Tandem reactions, also known as cascade reactions, typically involve at least two consecutive chemical transformations, with each subsequent reaction relying on the product of the previous one.[185] Integration of H_2O_2 electrosynthesis in tandem reactions allows on-site application of H_2O_2 or *in situ* generated ROS for subsequent chemical synthesis reactions, such as the oxidation of organic substrates.[186]

In general, most reactors can be integrated in tandem reactions, including flow-cells, PEMFCs and SE cells. The SE cells are the most commonly used, as they can produce high concentrations of pure H_2O_2, which ensures the purity of synthesized chemicals. The $2e^-$ ORR integrated tandem reactions can be implemented through two distinct modes: ex-cell mode and in-cell mode.[187] As illustrated in Fig. 13a, the ex-cell mode consists of two separated reaction processes: the pure H_2O_2 electrosynthesis in the SE cell and the oxidation of organic substrates in the tower reactor, which facilitates the application of on-site produced H_2O_2. The ex-cell mode could be regarded as an ordinary production process with the electrochemical and chemical steps conducted independently, thereby minimizing mutual interference and improving the tandem system reliability. For example, Fan *et al.*[127] developed a tandem reaction system using ex-cell mode for the synthesis of ethylene

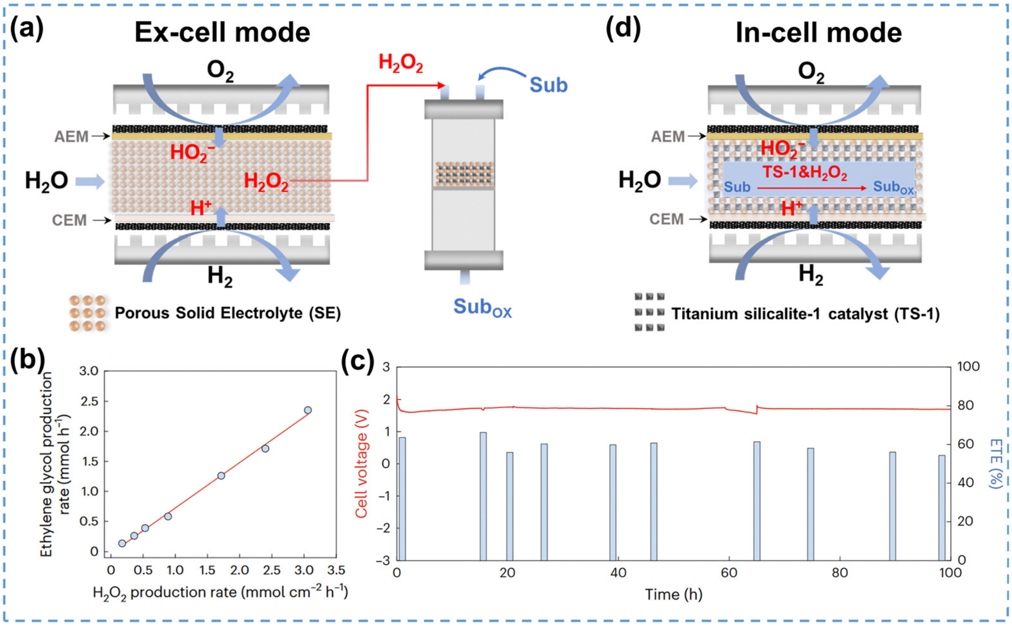

Fig. 13 (a) Schematic of ex-cell mode for $2e^-$ ORR integrated tandem reactions, adapted from ref. 127; (b) ethylene glycol production rate *vs.* H_2O_2 production rate, and (c) stability test for ethylene glycol production; (b) and (c) are reprinted with permission from ref. 127, copyright 2023, Springer Nature; (d) schematic of the in-cell mode for the $2e^-$ ORR integrated tandem reactions, adapted from ref. 188.

glycol under mild conditions. In this system, CNT-COOH served as the cathode to produce HO_2^-, and pure H_2O_2 was transferred into the subsequent tower reactor for the ethylene oxidation reaction. The ethylene glycol production rate correlated linearly with the H_2O_2 production rate with a slope of 0.75 (Fig. 13b), indicating that 75% of the electrochemically generated H_2O_2 had been utilized for ethylene glycol production. During the 100-hour stability test, the SE-cell voltage showed negligible decline, and the overall electron utilization efficiency was retained at $\sim$60%, exhibiting excellent stability (Fig. 13c).

However, tandem reactions using the ex-cell mode diminish the benefit of electrochemical *in situ* production of highly active H_2O_2 due to the separation between the electrochemical and chemical reaction steps. Moreover, the ex-cell mode is unable to make full use of the high concentration of H_2O_2 accumulated near the electrode surface to accelerate the subsequent reactions, as the highly concentrated H_2O_2 is usually diluted into the bulk solution before flowing to the downstream tower reactor. Zhang *et al.*[188] proposed an innovative in-cell mode based on SE cells, which incorporated the H_2O_2 electrosynthesis and the oxidation of organic substrates in a single integrated reactor. As illustrated in Fig. 13d, the middle layer of the reactor was filled with SE and TS-1 catalyst, which enabled multiple catalytic steps to proceed simultaneously. The feasibility of this novel in-cell tandem system was verified by the phenol oxidation reaction, which achieved 94.68% selectivity to target products (catechol and hydroquinone) under optimized conditions. This excellent catalytic performance was attributed to the full utilization of the *in situ* generated H_2O_2 and the direct activation of TS-1.

Although non-conductive TS-1 may increase the internal resistance of the reactor, the in-cell mode remains highly effective for chemical synthesis using *in situ* generated H_2O_2. We have summarized the applications of $2e^-$ ORR integrated tandem systems for chemical synthesis in the past three years in Table S4 (ESI†) for readers' reference. In the following sections, we will discuss the H_2O_2 concentration and ROS effects in this efficient tandem system mode with cutting-edge examples, and reveal its unique application values.

5.2 H_2O_2 concentration effect in the in-cell mode

During the $2e^-$ ORR at the electrode, the produced H_2O_2 will accumulate near the electrode surface region, leading to a significantly higher H_2O_2 concentration compared to the bulk solution.[34,189] In batch H_2O_2 electrosynthesis, the elevated concentration near the electrode surface region can initiate undesired H_2O_2RRs.[101] However, H_2O_2 in tandem reaction systems is directly used as an intermediate oxidizing agent, therefore the high H_2O_2 concentration near the electrode surface will facilitate subsequent organic substrate oxidation reactions.

The H_2O_2 concentration effect in the SE cell was first demonstrated by Zhang *et al.*,[34] by visualization of the H_2O_2 concentration gradient between the electrode surface region and the bulk region using finite element simulations. Apparently, a sharp increase in H_2O_2 concentration up to 2.06 wt% was observed near the electrode, which was 25 times higher than the average concentration in the bulk solution (0.08 wt%), as shown in Fig. 14a. Using the ethylene epoxidation reaction as the model reaction, the in-cell mode SE reactor (Fig. 14b) significantly enhanced ethylene epoxidation rate, and tripled glycol yield compared to the ex-cell mode. This reactor maintained a 99.7% selectivity for ethylene glycol production over 200 hours, demonstrating excellent stability and high application potential.

To maximize the utilization of the H_2O_2 concentration effect for high-value chemical synthesis, the organic oxidation catalysts (*e.g.* TS-1) should be closely distributed on the electrode surface region. Liu *et al.*[190] prepared a bifunctional electrode by mixing nanoscale TS-1 with oxygen-doped carbon catalyst (C–O), which ensured both effective H_2O_2 electrosynthesis and the activation of TS-1 by H_2O_2 near the electrode. Fig. 14c illustrated a simple flow-cell reactor for ethylene epoxidation reaction using the bifunctional electrode, which produced propylene glycol with 80% selectivity and achieved a yield of 4.28 mmol h^{-1} $g_{catalyst}{}^{-1}$ when the mass ratio of C–O : TS-1 was adjusted to 1 : 3.

PEMFCs have been increasingly explored for the production of high-value chemicals, and current research studies primarily focus on the direct electrocatalytic reactions involving precious metal catalysts.[192] As discussed in Section 4.1.3, the electrosynthesis of H_2O_2 *via* PEMFCs faces the dilemma of H_2O_2 transport within the zero-gap MEA, which hinders the batch H_2O_2 electrosynthesis. Luckily, the H_2O_2 concentration effect can turn this disadvantage into an advantage, as the high concentration of H_2O_2 accumulated by MEA can be directly utilized in tandem reactions to produce high-value chemicals. As depicted in Fig. 14d, Yang *et al.*[191] developed a new strategy to oxidize propane by utilizing the high concentration of H_2O_2 in PEMFCs. The cathode was constructed by a $2e^-$ ORR catalyst and propane oxidation catalyst MIL-53 (Al, Fe). Under mild reaction conditions (80 °C), the propane oxidation was significantly enhanced by the high concentration of H_2O_2 in the zero-gap MEA, achieving a yield of 11.4 mmol L^{-1} h^{-1} of C_3 oxygenates, which was approximately ten times higher than that reported in direct alkane oxidization at the PEMFC anode.

5.3 ROS effect in the in-cell mode

The *in situ* generated H_2O_2 could also decompose to produce ROS, such as superoxide radicals ($^\bullet O_2^-$), hydroxyl radicals ($^\bullet OH$), and hydroperoxyl radicals ($^\bullet OOH$),[193] which typically exhibit stronger oxidizing ability compared to H_2O_2, thus accelerating organic substrate oxidation reactions. The ROS effect in the in-cell mode will bring more opportunities for chemical synthesis, especially for reactants that are difficult to activate, such as methane (CH_4) and nitrogen (N_2).

Taking the CH_4 oxidation reaction as an example, converting CH_4 into high-value liquid oxygenates typically requires harsh conditions of high temperatures and pressures.[194] Kim *et al.*[195] proposed a strategy for the partial oxidation of CH_4 using ROS generated by electro-synthesized H_2O_2 under ambient conditions. As illustrated in Fig. 15a, H_2O_2 was synthesized on a carbon electrode and subsequently activated to generate ROS to participate in the CH_4 oxidation reaction. The further

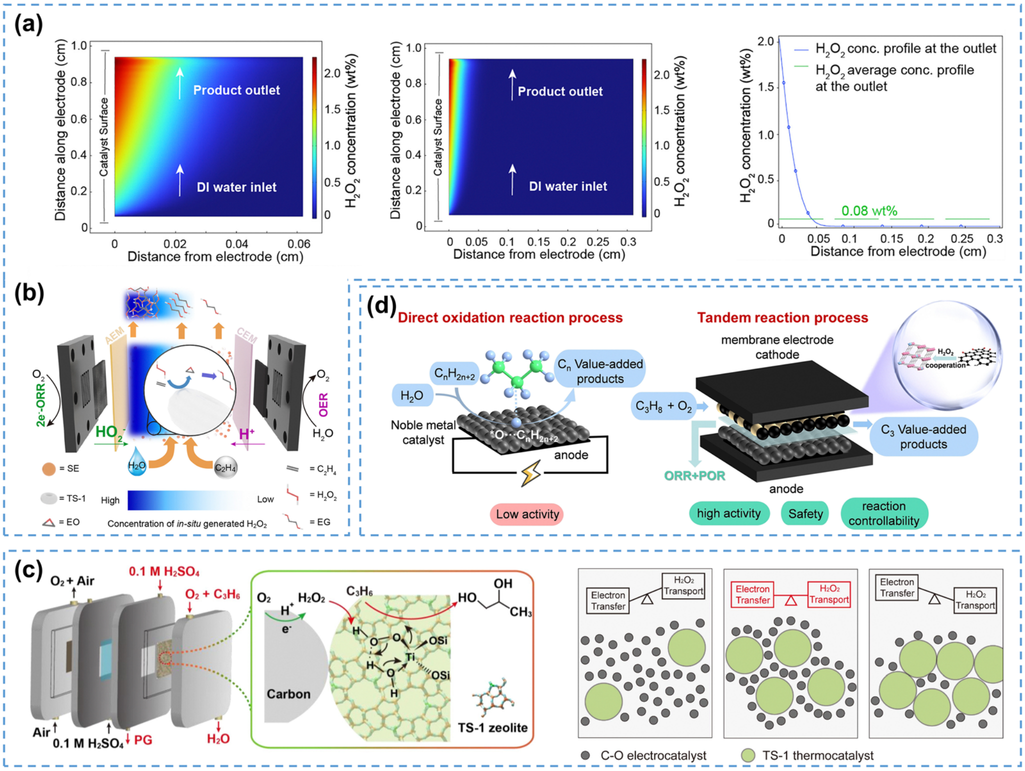

Fig. 14 (a) Finite element simulations of the interfacial H_2O_2 concentration and the bulk solution concentration, and (b) schematic of the integrated SE reactor; (a) and (b) are reprinted with permission from ref. 34, copyright 2023, Elsevier; (c) schematic of the flow-cell with a bifunctional electrode for the propylene oxidation reaction, reprinted with permission from ref. 190, copyright 2023, Elsevier; (d) schematic of direct electrochemical oxidation of alkane (left), and a tandem reaction process for alkane oxidation in PEMFCs (right), reprinted with permission from ref. 191, copyright 2023, Wiley-VCH.

mechanistic study revealed that H_2O_2 could not react with CH_4 directly, whereas ROS (*e.g.* $^\bullet$OH and $^\bullet$OOH radicals) generated by H_2O_2 significantly activated CH_4, forming a series of liquid oxygenates such as CH_3OH, CH_3OOH, and HCOOH. This system achieved a high selectivity (80.7%) and production rate (18.9 μmol h^{-1}) for converting CH_4 to HCOOH under ambient conditions (Fig. 15b), offering a new method for the direct partial oxidation of CH_4.

It has been demonstrated that oxygen functional groups in carbon materials favor the generation of $^\bullet$OH from H_2O_2 in acidic media.[198,199] Lin *et al.*[200] developed an oxygen-rich carbon electrode, which facilitated the oxidation of acetic acid to peroxyacetic acid due to abundant $^\bullet$OH radicals activated from H_2O_2.

The electro-Fenton reaction is a well-known process that can effectively activate H_2O_2 to generate ROS. In this process, Fe^{2+} reacts with H_2O_2 to produce $^\bullet$OH and Fe^{3+}, and the Fe^{3+} is reduced back to Fe^{2+} at the cathode, forming a continuous cyclic conversion of the Fe^{2+}/Fe^{3+} redox pair.[201] Chen *et al.*[196] successfully oxidized N_2 to HNO_3 using $^\bullet$OH generated by the electro-Fenton reaction. As illustrated in Fig. 15c, O_2 was reduced to H_2O_2 on the graphite electrode and further converted into $^\bullet$OH by Fe^{2+}. The $^\bullet$OH is a strong nucleophile reagent, which activated N_2 and produced HNO_3. This tandem reaction system demonstrated good stability over ten reaction cycles, maintaining a faradaic efficiency of ~25% and a HNO_3 yield of 140 μmol h^{-1} g_{Fe}^{-1} (Fig. 15d).

In the above examples, ROS directly interact with organic substrates to produce high-value chemicals, while in most cases, catalysts such as TS-1 are indispensable to catalyze the organic substrate oxidation reactions. Therefore, it is essential to explore the interaction between the catalysts and ROS in tandem reactions. The ROS directly transferred to near the TS-1 catalyst, forming the active Ti-OOH species, which accelerated the reaction kinetics of the ethylene oxidation reaction.[202] Yuan *et al.*[197] proposed that the direct generation of active Ti-OOH species from the interaction between $^\bullet$OOH radicals and the Ti-MOR catalyst was the primary pathway (pathway II) in the tandem system (Fig. 15e). Further application using the GDE reactor, equipped with external catholyte containing Ti-MOR catalyst (Fig. 15f), converted CYC (60 mM) to oxime (57 mM) with a yield of 95% at a current of 60 mA.

6 Summaries and prospects

The decentralized production of H_2O_2 *via* the $2e^-$ ORR is an important method for clean and sustainable synthesis of H_2O_2, offering a green, safe and energy-efficient alternative to the anthraquinone process. The aspects of H_2O_2 electrosynthesis beyond catalysts have been discussed in this review, with a particular focus on the reactor design and its integration into tandem systems.

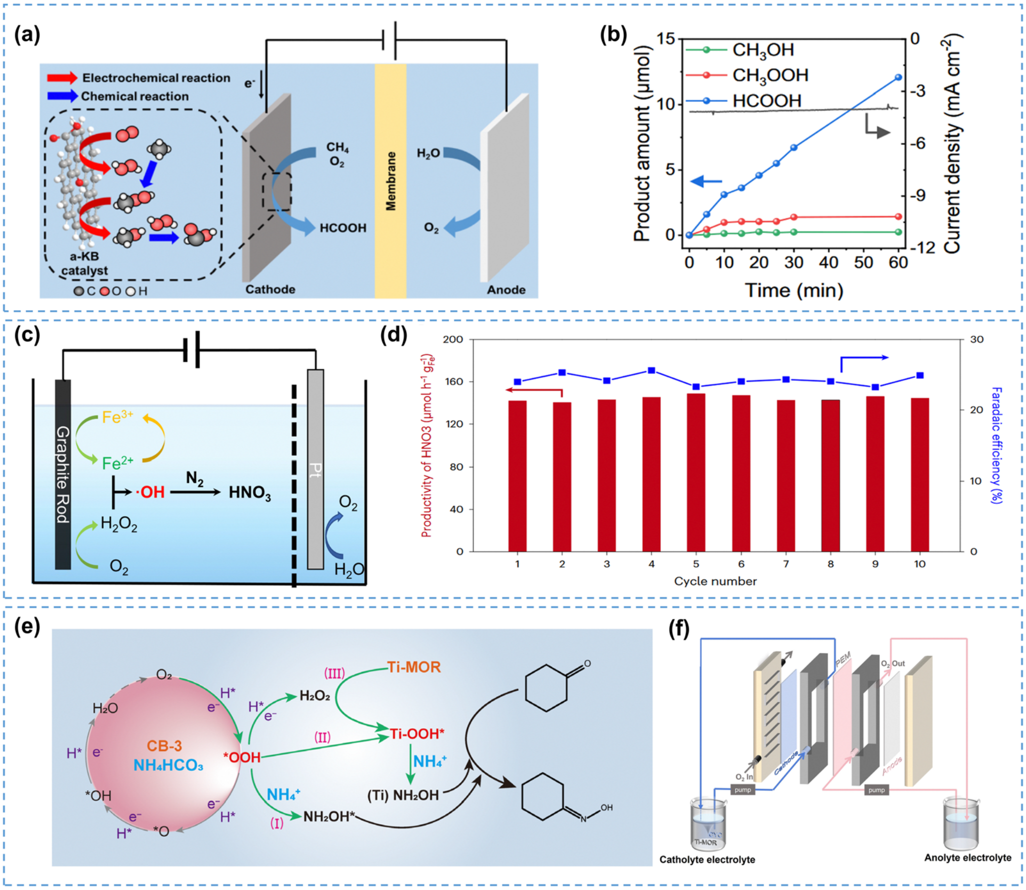

Fig. 15 (a) Schematic of the electro-assisted CH_4 partial oxidation process, and (b) production rates of liquid products; (a) and (b) are reprinted with permission from ref. 195, copyright 2023, Springer Nature; (c) schematic of N_2 oxidation using electro-Fenton generated $^{\bullet}OH$, and (d) performance of the graphite rod cathode over ten reaction cycles; (c) and (d) are reprinted with permission from ref. 196, copyright 2023, Springer Nature; (e) schematic of the proposed pathways for the CYC oximation in the $2e^-$ ORR integrated system, and (f) flow-cell reactor for CYC oximation; (e) and (f) are reprinted with permission from ref. 197, copyright 2024, American Association for the Advancement of Science.

Various aspects in reactor design have been discussed, including electrode surface/interface modifications and designs for cell configurations. Firstly, by discussing the surface wettability of carbon electrodes, it is suggested that an electrode surface with appropriate hydrophobicity is preferred to enhance the overall performance. Subsequently, the strategies for controlling the carbon electrode–electrolyte interface microenvironment have been reviewed. By reducing the proton concentration at the electrode interface or slowing the proton transfer rate, the H_2O_2RR can be effectively inhibited, thus enhancing the H_2O_2 production. Additionally, enhancing the electric field can improve the stability of $2e^-$ ORR intermediates, and boost H_2O_2 electrosynthesis. Furthermore, the optimizations of key reactor components, as well as the challenges in practical-scale H_2O_2 electrosynthesis, have been summarized, revealing that optimized FFP and EC structures can enhance the overall performance. In the last part, we focus on the applications of the $2e^-$ ORR by integrating it into tandem systems for value-added chemical synthesis. The H_2O_2 concentration and ROS effects in $2e^-$ ORR integrated tandem reactions have been discussed in detail. Despite recent advances in electrodes and reactors for improved H_2O_2 electrosynthesis, challenges still remain in achieving large-scale H_2O_2 production, and future studies may focus on the following aspects:

(1) Investigate the dynamic evolution of three-phase interfaces (TPIs). The stable TPIs are determining factors on the electrode activity, stability and H_2O_2 selectivity in the application of GDE-based reactors. Currently, the states of the TPIs are generally represented by the three wetting states on the electrode, which are simply evaluated by measuring the contact angle before and post reaction. 3D images and dynamic evolution of TPIs are greatly needed for a better understanding of the construction of TPIs. The utilization of confocal laser scanning microscopy, micro-computed tomography 3D imaging, and environmental scanning electron microscopy could provide valuable insights into the reaction mechanisms and construction of durable TPIs.

(2) Investigate the cation effect on the $2e^-$ ORR comprehensively. Although previous studies suggest that cations create an alkaline-like microenvironment, which is beneficial for H_2O_2 electrosynthesis, researchers indicate that a localized alkaline-like microenvironment can be formed without cation addition,[203,204] particularly at higher current densities due to significant proton consumption. Other researchers ascribe the

enhanced H_2O_2 electrosynthesis performance to the AMC-induced electric field modification,[106] however, this effect has not been validated at larger current densities. The effect of AMC on H_2O_2 electrosynthesis can be rather complicated, and future studies should explore the comprehensive effects of cations, including their influences on interface electric fields and H-bond networks, and further verify the universality of the cation effects on different types of catalysts.

(3) Investigate the dynamic evolution of catalysts under *operando* conditions. The harsh oxidative conditions during the $2e^-$ ORR can potentially alter catalyst structure and accelerate the degradation process. Designing and developing novel catalysts require a thorough evaluation of their resistance to oxidative conditions, as well as their evolution mechanisms. Advanced *operando* characterizations are needed, such as *in situ* Raman spectroscopy and *operando* EXAFS characterization, which enable real-time monitoring of catalyst structures. Understanding of the catalyst evolution under *operando* conditions will provide valuable insights into the fundamental aspects in material science and guide the design and development of efficient and durable electrocatalysts.

(4) Explore more application scenarios for *in situ* generated H_2O_2. A particularly promising direction is to incorporate chemical feedstocks into $2e^-$ ORR integrated tandem systems to synthesize high-value chemicals, which represents sustainable and environmentally-friendly pathways. Integrating H_2O_2 electrosynthesis with other chemical reaction systems not only enhances energy efficiency but also enables the production of more complex chemical compounds under mild conditions. Recently, Kong *et al.*[205] demonstrated a groundbreaking approach by integrating three electrolysis systems—CO_2RR, nitrogen reduction reaction (NRR), and $2e^-$ ORR—to achieve the green synthesis of glycine, a key amino acid. Moving forward, reactor designs should focus on tailoring systems for specific applications, thereby maximizing the utilization efficiency of H_2O_2 and contributing to sustainable chemical processes.

(5) Assess the economic feasibility and perform lifecycle analyses of H_2O_2 electrosynthesis and $2e^-$ ORR integrated tandem systems. A comprehensive techno-economic analysis should evaluate product efficiency, scalability, and lifecycle impacts, and ultimately guide the development of cost-effective, resource-efficient, and sustainable chemical production processes. The analyses should include not only direct economic costs, such as pre-investments and electricity consumption, but also include the environmental costs, with a particular emphasis on carbon emissions and their environmental impacts.

Data availability

No primary research results, software or code have been included and no new data have been generated or analyzed in this review.

Conflicts of interest

There are no conflicts of interest to declare.

Acknowledgements

The authors are thankful for the financial support from the National Natural Science Foundation of China (grant number 22172112) and the Fundamental Research Funds for the Central Universities.

References

1 R. L. Myers, *The 100 Most Important Chemical Compounds: A Reference Guide*, Greenwood Press, 2007.
2 X. Wen, X. Zhang, M. Wang, C. Yuan, J. Lang, X. Li, H. Wei, D. Mandler and M. Long, *Appl. Catal., B*, 2024, **342**, 123437.
3 C. Xia, Y. Xia, P. Zhu, L. Fan and H. Wang, *Science*, 2019, **366**, 226–231.
4 M. Wang, J. Cheng, W. Xu, D. Zhu, W. Zhang, Y. Wen, W. Guan, J. Jia and Z. Lu, *Nat. Nanotechnol.*, 2024, **20**, 67–74.
5 M. Lu, X. Liu, C. Jing, X. Wang, L. Ding, F. Gao, L. Ren, S. Dai, X. Zhong and J. Wang, *Adv. Funct. Mater.*, 2024, 2412170.
6 S. Yang, A. Verdaguer-Casadevall, L. Arnarson, L. Silvioli, V. Čolić, R. Frydendal, J. Rossmeisl, I. Chorkendorff and I. E. L. Stephens, *ACS Catal.*, 2018, **8**, 4064–4081.
7 S. C. Perry, D. Pangotra, L. Vieira, L.-I. Csepei, V. Sieber, L. Wang, C. Ponce de León and F. C. Walsh, *Nat. Rev. Chem.*, 2019, **3**, 442–458.
8 A. Byeon, W. C. Yun, J. M. Kim and J. W. Lee, *ChemElectroChem*, 2023, **10**, e202300234.
9 Y. Tian, D. Deng, L. Xu, M. Li, H. Chen, Z. Wu and S. Zhang, *Nano-Micro Lett.*, 2023, **15**, 122.
10 D. Zhang, E. Mitchell, X. Lu, D. Chu, L. Shang, T. Zhang, R. Amal and Z. Han, *Mater. Today*, 2023, **63**, 339–359.
11 S. Siahrostami, A. Verdaguer-Casadevall, M. Karamad, D. Deiana, P. Malacrida, B. Wickman, M. Escudero-Escribano, E. A. Paoli, R. Frydendal, T. W. Hansen, I. Chorkendorff, I. E. L. Stephens and J. Rossmeisl, *Nat. Mater.*, 2013, **12**, 1137–1143.
12 M. Huang, Z. Cui, Z. Li and W. Sheng, *ACS Catal.*, 2024, **14**, 2095–2106.
13 Z. Yu, H. Deng, Q. Yao, L. Zhao, F. Xue, T. He, Z. Hu, W.-H. Huang, C.-W. Pao, L.-M. Yang and X. Huang, *Nat. Commun.*, 2024, **15**, 9346.
14 H. Li, P. Wen, D. S. Itanze, Z. D. Hood, S. Adhikari, C. Lu, X. Ma, C. Dun, L. Jiang, D. L. Carroll, Y. Qiu and S. M. Geyer, *Nat. Commun.*, 2020, **11**, 3928.
15 Q. Sun, G. Xu, B. Xiong, L. Chen and J. Shi, *Nano Res.*, 2023, **16**, 4729–4735.
16 X.-L. Zhang, X. Su, Y.-R. Zheng, S.-J. Hu, L. Shi, F.-Y. Gao, P.-P. Yang, Z.-Z. Niu, Z.-Z. Wu, S. Qin, R. Wu, Y. Duan, C. Gu, X.-S. Zheng, J.-F. Zhu and M.-R. Gao, *Angew. Chem., Int. Ed.*, 2021, **60**, 26922–26931.
17 W. Liu, R. Chen, Z. Sang, Z. Li, J. Nie, L. Yin, F. Hou and J. Liang, *Adv. Mater.*, 2024, **36**, 2406403.
18 S. Chen, T. Luo, J. Wang, J. Xiang, X. Li, C. Ma, C.-W. Kao, T.-S. Chan, Y.-N. Liu and M. Liu, *Angew. Chem., Int. Ed.*, 2024, e202418713.

19 H. Huang, M. Sun, S. Li, S. Zhang, Y. Lee, Z. Li, J. Fang, C. Chen, Y.-X. Zhang, Y. Wu, Y. Che, S. Qian, W. Zhu, C. Tang, Z. Zhuang, L. Zhang and Z. Niu, *J. Am. Chem. Soc.*, 2024, **146**, 9434–9443.

20 J. Du, G. Han, W. Zhang, L. Li, Y. Yan, Y. Shi, X. Zhang, L. Geng, Z. Wang, Y. Xiong, G. Yin and C. Du, *Nat. Commun.*, 2023, **14**, 4766.

21 C. Zhang, W. Shen, K. Guo, M. Xiong, J. Zhang and X. Lu, *J. Am. Chem. Soc.*, 2023, **145**, 11589–11598.

22 Y. Long, J. Lin, F. Ye, W. Liu, D. Wang, Q. Cheng, R. Paul, D. Cheng, B. Mao, R. Yan, L. Zhao, D. Liu, F. Liu and C. Hu, *Adv. Mater.*, 2023, **35**, e2303905.

23 Z. Lin, C. Han, G. E. P. O'Connell and X. Lu, *Angew. Chem., Int. Ed.*, 2023, **62**, e202301435.

24 Y. Wen, T. Zhang, J. Wang, Z. Pan, T. Wang, H. Yamashita, X. Qian and Y. Zhao, *Angew. Chem., Int. Ed.*, 2022, **61**, e202205972.

25 N. Li, C. Huang, X. Wang, Y. Feng and J. An, *Chem. Eng. J.*, 2022, **450**, 138246.

26 X. Zhang, X. Zhao, P. Zhu, Z. Adler, Z.-Y. Wu, Y. Liu and H. Wang, *Nat. Commun.*, 2022, **13**, 2880.

27 J. L. Hübner, L. E. B. Lucchetti, H. N. Nong, D. I. Sharapa, B. Paul, M. Kroschel, J. Kang, D. Teschner, S. Behrens, F. Studt, A. Knop-Gericke, S. Siahrostami and P. Strasser, *ACS Energy Lett.*, 2024, **9**, 1331–1338.

28 T. Burdyny and W. A. Smith, *Energy Environ. Sci.*, 2019, **12**, 1442–1453.

29 L. Cui, B. Chen, D. Chen, C. He, Y. Liu, H. Zhang, J. Qiu, L. Liu, W. Jing and Z. Zhang, *Nat. Commun.*, 2024, **15**, 10632.

30 B. Ni, P. Shen, G. Zhang, J. Zhao, H. Ding, Y. Ye, Z. Yue, H. Yang, H. Wei and K. Jiang, *J. Am. Chem. Soc.*, 2024, **146**, 11181–11192.

31 Z. Xing, L. Hu, D. S. Ripatti, X. Hu and X. Feng, *Nat. Commun.*, 2021, **12**, 136.

32 C. Ni, W. Xu, N. Deng and X. Huang, *J. Cleaner Prod.*, 2024, **480**, 144066.

33 Y. Ma, E. Zhao, G. Xia, J. Zhan, G. Yu and Y. Wang, *Water Res.*, 2023, **229**, 119503.

34 S.-K. Zhang, Y. Feng, A. Elgazzar, Y. Xia, C. Qiu, Z. Adler, C. Sellers and H. Wang, *Joule*, 2023, **7**, 1887–1901.

35 J. Kim, J. H. Kim, C. Oh, H. Yun, E. Lee, H.-S. Oh, J. H. Park and Y. J. Hwang, *Nat. Commun.*, 2023, **14**, 4704.

36 S. Chen, S. Liang, R. Huang, M. Zhang, Y. Song, Y. Zhang, S. Tao, L. Yu and D. Deng, *Nat. Synth.*, 2024, **3**, 76–84.

37 Z. Lu, G. Chen, S. Siahrostami, Z. Chen, K. Liu, J. Xie, L. Liao, T. Wu, D. Lin, Y. Liu, T. F. Jaramillo, J. K. Nørskov and Y. Cui, *Nat. Catal.*, 2018, **1**, 156–162.

38 C. Xia, J. Y. Kim and H. Wang, *Nat. Catal.*, 2020, **3**, 605–607.

39 J. S. Choi, G. V. Fortunato, D. C. Jung, J. C. Lourenco, M. R. V. Lanza and M. Ledendecker, *Nanoscale Horiz.*, 2024, **9**, 1250–1261.

40 R. Zhou, Y. Zheng, M. Jaroniec and S.-Z. Qiao, *ACS Catal.*, 2016, **6**, 4720–4728.

41 P. Wang, T. Hayashi, Q. Meng, Q. Wang, H. Liu, K. Hashimoto and L. Jiang, *Small*, 2017, **13**, 1601250.

42 Y. Wang, Y. Zou, L. Tao, Y. Wang, G. Huang, S. Du and S. Wang, *Nano Res.*, 2019, **12**, 2055–2066.

43 Y. He, S. Liu, M. Wang, Q. Cheng, T. Qian and C. Yan, *J. Energy Chem.*, 2023, **80**, 302–323.

44 K. Shi, Z. Ren, Z. Meng and X. Feng, *ChemCatChem*, 2024, **16**, e202301308.

45 G. Xia, Y. Tian, X. Yin, W. Yuan, X. Wu, Z. Yang, G. Yu, Y. Wang and M. Wu, *Appl. Catal., B*, 2021, **299**, 120655.

46 Z. Xing, K. Shi, Z. S. Parsons and X. Feng, *ACS Catal.*, 2023, **13**, 2780–2789.

47 J. Ryu and D. W. Lee, *J. Mater. Chem. A*, 2024, **12**, 10012–10043.

48 C. Zhang, Z. Xu, N. Han, Y. Tian, T. Kallio, C. Yu and L. Jiang, *Sci. Adv.*, 2024, **9**, eadd6978.

49 H. Yang, Y. Liu, X. Liu, X. Wang, H. Tian, G. I. N. Waterhouse, P. E. Kruger, S. G. Telfer and S. Ma, *eScience*, 2022, **2**, 227–234.

50 K. Dong, J. Liang, Y. Wang, Z. Xu, Q. Liu, Y. Luo, T. Li, L. Li, X. Shi, A. M. Asiri, Q. Li, D. Ma and X. Sun, *Angew. Chem., Int. Ed.*, 2021, **60**, 10583–10587.

51 X. You, F. Hou, T. Xie, A. Cai, H. He, G. Li, F. Zhang, W. Peng, X. Fan and Y. Li, *J. Colloid Interface Sci.*, 2023, **639**, 333–342.

52 R. T. Ferrell and D. M. Himmelblau, *J. Chem. Eng. Data*, 1967, **12**, 111–115.

53 B. Carnes and N. Djilali, *J. Power Sources*, 2005, **144**, 83–93.

54 Z. Liu, K. Li, L. Liu, H. Song, Y. Zhang, M. Tebyetekerwa, X. Zhang, K. Wang, L. Xu and J. Wang, *Appl. Catal., B*, 2024, **357**, 124311.

55 J. Wang, C. Li, M. Rauf and W. Wang, *ACS Sustainable Chem. Eng.*, 2022, **11**, 436–443.

56 K. Wang and M. Pera-Titus, *Sci. Adv.*, 2024, **10**, eado5448.

57 Q. Zhang, M. Zhou, G. Ren, Y. Li, Y. Li and X. Du, *Nat. Commun.*, 2020, **11**, 1731.

58 B. Hu, M. Wang, D. Li, J. Chen, C. Li and L. Wang, *Adv. Energy Sustainability Res.*, 2023, **4**, 230014.

59 J. Chen, H. Qiu, Y. Zhao, H. Yang, L. Fan, Z. Liu, S. Xi, G. Zheng, J. Chen, L. Chen, Y. Liu, L. Guo and L. Wang, *Nat. Commun.*, 2024, **15**, 5893.

60 P. Xia, L. Zhao, X. Chen, Z. Ye, Z. Zheng, Q. He and I. Sirés, *Appl. Catal., B*, 2024, **343**, 123467.

61 F. Yu, M. Zhou and X. Yu, *Electrochim. Acta*, 2015, **163**, 182–189.

62 Y. Qiao, N. Ren, X. Li, J. An, X. Wang and N. Li, *Chem. Eng. J.*, 2023, **463**, 142417.

63 B. Sabri Rawah, M. Albloushi and W. Li, *Chem. Eng. J.*, 2023, **466**, 143282.

64 H. Wang, S. Jiang, H. Yu, K. Deng, Z. Wang, X. Li, Y. Xu and L. Wang, *J. Mater. Chem. A*, 2023, **11**, 13633–13639.

65 P. Cao, X. Quan, K. Zhao, X. Zhao, S. Chen and H. Yu, *ACS Catal.*, 2021, **11**, 13797–13808.

66 H. Xu, X. H. Lv, H. Y. Wang, J. Y. Ye, J. Yuan, Y. C. Wang, Z. Y. Zhou and S. G. Sun, *ChemSusChem*, 2022, **15**, e202102587.

67 B. L. French, J. J. Wang, M. Y. Zhu and B. C. Holloway, *Thin Solid Films*, 2006, **494**, 105–109.

68 J. Wang, M. Zhu, R. A. Outlaw, X. Zhao, D. M. Manos and B. C. Holloway, *Carbon*, 2004, **42**, 2867–2872.

69 L. X. Zhang, Z. Sun, J. L. Qi, J. M. Shi, T. D. Hao and J. C. Feng, *Carbon*, 2016, **103**, 339–345.

70 Y. Wang, R. Shi, L. Shang, L. Peng, D. Chu, Z. Han, G. I. N. Waterhouse, R. Zhang and T. Zhang, *Nano Energy*, 2022, **96**, 107046.

71 D. Zhang, C. Tsounis, Z. Ma, D. Djaidiguna, N. M. Bedford, L. Thomsen, X. Lu, D. Chu, R. Amal and Z. Han, *Small*, 2022, **18**, e2105082.

72 A. Kozbial, F. Zhou, Z. Li, H. Liu and L. Li, *Acc. Chem. Res.*, 2016, **49**, 2765–2773.

73 D. Zhang, C. Tsounis, Z. Ma, L. Peng, Z. Lin, H. Yin, F. Hussain, C. Cazorla, D. Chu, R. Amal and Z. Han, *Cell Rep. Phys. Sci.*, 2023, **4**, 101643.

74 F. Mugele and J.-C. Baret, *J. Phys.: Condens. Matter*, 2005, **17**, R705.

75 L. Cui, B. Chen, L. Zhang, C. He, C. Shu, H. Kang, J. Qiu, W. Jing, K. Ostrikov and Z. Zhang, *Energy Environ. Sci.*, 2024, **17**, 655–667.

76 J. Chen, H. Qiu, Y. Zhao, H. Yang, L. Fan, Z. Liu, S. Xi, G. Zheng, J. Chen, L. Chen, Y. Liu, L. Guo and L. Wang, *Nat. Commun.*, 2024, **15**, 5893.

77 R. Haaring, P. W. Kang, J. W. Lee, J. Lee and H. Lee, *ACS Appl. Mater. Interfaces*, 2024, **16**, 28731–28741.

78 Y. Sheng, Y. Zhao, X. Wang, R. Wang and T. Tang, *Electrochim. Acta*, 2014, **133**, 414–421.

79 K. Yang, R. Kas, W. A. Smith and T. Burdyny, *ACS Energy Lett.*, 2021, **6**, 33–40.

80 Y. J. Sa, C. W. Lee, S. Y. Lee, J. Na, U. Lee and Y. J. Hwang, *Chem. Soc. Rev.*, 2020, **49**, 6632–6665.

81 J. Wu, *Chem. Rev.*, 2022, **122**, 10821–10859.

82 T. Kumeda and K. Sakaushi, *Curr. Opin. Electrochem.*, 2022, **36**, 101121.

83 P. Sebastián-Pascual, Y. Shao-Horn and M. Escudero-Escribano, *Curr. Opin. Electrochem.*, 2022, **32**, 100918.

84 M. M. Waegele, C. M. Gunathunge, J. Li and X. Li, *J. Chem. Phys.*, 2019, **151**, 160902.

85 J. L. Hubner, L. E. B. Lucchetti, H. N. Nong, D. I. Sharapa, B. Paul, M. Kroschel, J. Kang, D. Teschner, S. Behrens, F. Studt, A. Knop-Gericke, S. Siahrostami and P. Strasser, *ACS Energy Lett.*, 2024, **9**, 1331–1338.

86 X. Zhang, X. Zhao, P. Zhu, Z. Adler, Z. Y. Wu, Y. Liu and H. Wang, *Nat. Commun.*, 2022, **13**, 2880.

87 D. Park and Y. Jung, *Chem Catal.*, 2024, **4**, 100823.

88 X. Y. Li, T. Wang, Y. C. Cai, Z. D. Meng, J. W. Nan, J. Y. Ye, J. Yi, D. P. Zhan, N. Tian, Z. Y. Zhou and S. G. Sun, *Angew. Chem., Int. Ed.*, 2023, **62**, e202218669.

89 P. Cao, X. Zhao, Y. Liu, H. Zhang, K. Zhao, S. Chen, H. Yu, F. Dong, N. N. Nichols, J. G. Chen and X. Quan, *Angew. Chem., Int. Ed.*, 2024, **63**, e202406452.

90 Y. Fan, Y. Chen, W. Ge, L. Dong, Y. Qi, C. Lian, X. Zhou, H. Liu, Z. Liu, H. Jiang and C. Li, *J. Am. Chem. Soc.*, 2024, **146**, 7575–7583.

91 Y. Fang, Y. Fan, K. Xie, W. Ge, Y. Zhu, Z. Qi, Z. Song, H. Jiang and C. Li, *Angew. Chem., Int. Ed.*, 2023, **62**, e202304413.

92 E. L. Gyenge and C. W. Oloman, *J. Appl. Electrochem.*, 2001, **31**, 233–243.

93 G. A. Kolyagin and V. L. Kornienko, *Russ. J. Appl. Chem.*, 2006, **79**, 746–751.

94 P. Li, Y. Jiang, Y. Hu, Y. Men, Y. Liu, W. Cai and S. Chen, *Nat. Catal.*, 2022, **5**, 900–911.

95 Q. Nian, X. Zhang, Y. Feng, S. Liu, T. Sun, S. Zheng, X. Ren, Z. Tao, D. Zhang and J. Chen, *ACS Energy Lett.*, 2021, **6**, 2174–2180.

96 Y. Fang, Y. Fan, K. Xie, W. Ge, Y. Zhu, Z. Qi, Z. Song, H. Jiang and C. Li, *Angew. Chem., Int. Ed.*, 2023, **62**, e202304413.

97 C. Yang, F. Sun, Z. Qu, X. Li, W. Zhou and J. Gao, *ACS Energy Lett.*, 2022, **7**, 4398–4407.

98 L. Jing, Q. Tian, W. Wang, X. Li, Q. Hu, H. Yang and C. He, *Adv. Energy Mater.*, 2024, **14**, 2304418.

99 Q. Tian, L. Jing, Y. Yin, Z. Liang, H. Du, L. Yang, X. Cheng, D. Zuo, C. Tang, Z. Liu, J. Liu, J. Wan and J. Yang, *Nano Lett.*, 2024, **24**, 1650–1659.

100 Q. Tian, L. Jing, H. Du, Y. Yin, X. Cheng, J. Xu, J. Chen, Z. Liu, J. Wan, J. Liu and J. Yang, *Nat. Commun.*, 2024, **15**, 983.

101 K.-H. Wu, D. Wang, X. Lu, X. Zhang, Z. Xie, Y. Liu, B.-J. Su, J.-M. Chen, D.-S. Su, W. Qi and S. Guo, *Chem*, 2020, **6**, 1443–1458.

102 S. Zhao, Y. Wang, Y. Hao, L. Yin, C. H. Kuo, H. Y. Chen, L. Li and S. Peng, *Adv. Mater.*, 2024, **36**, e2308925.

103 J. Guo, Y. Zheng, Z. Hu, C. Zheng, J. Mao, K. Du, M. Jaroniec, S.-Z. Qiao and T. Ling, *Nat. Energy*, 2023, **8**, 264–272.

104 H. Li, P. Cao, H. Zhang, K. Wang, S. Chen, H. Yu and X. Quan, *Chem. Eng. J.*, 2024, **497**, 154523.

105 S. R. Kelly, C. Kirk, K. Chan and J. K. Nørskov, *J. Phys. Chem. C*, 2020, **124**, 14581–14591.

106 J. Lee, J. S. Lim, G. Yim, H. Jang, S. H. Joo and Y. J. Sa, *ACS Appl. Mater. Interfaces*, 2021, **13**, 59904–59914.

107 Y. Ding, W. Zhou, L. Xie, S. Chen, J. Gao, F. Sun, G. Zhao and Y. Qin, *J. Mater. Chem. A*, 2021, **9**, 15948–15954.

108 J. Yu, J. Yin, R. Li, Y. Ma and Z. Fan, *Chem Catal.*, 2022, **2**, 2229–2252.

109 B. Pan, Y. Wang and Y. Li, *Chem Catal.*, 2022, **2**, 1267–1276.

110 J. Chen, Y. Zhao, H. Yang, T. Zhang, L. Fan, C. Li and L. Wang, *Nanoscale*, 2023, **15**, 3832–3840.

111 K. Zhou and L. Li, *J. Alloys Compd.*, 2024, **1002**, 175549.

112 M. Liu, Y. Pang, B. Zhang, P. De Luna, O. Voznyy, J. Xu, X. Zheng, C. T. Dinh, F. Fan, C. Cao, F. P. de Arquer, T. S. Safaei, A. Mepham, A. Klinkova, E. Kumacheva, T. Filleter, D. Sinton, S. O. Kelley and E. H. Sargent, *Nature*, 2016, **537**, 382–386.

113 Y. Ding, W. Zhou, J. Li, J. Wang, L. Xie, X. Meng, J. Gao, F. Sun, G. Zhao and Y. Qin, *ACS Energy Lett.*, 2023, **8**, 3122–3130.

114 W. Shen, C. Zhang, M. Alomar, Z. Du, Z. Yang, J. Wang, G. Xu, J. Zhang, J. Lv and X. Lu, *Nano Res.*, 2023, **17**, 1217–1224.

115 W. Shen, C. Zhang, X. Wang, Y. Huang, Z. Du, M. Alomar, J. Wang, J. Lv, J. Zhang and X. Lu, *ACS Mater. Lett.*, 2023, **6**, 17–26.

116 Z. Mou, Y. Mu, L. Liu, D. Cao, S. Chen, W. Yan, H. Zhou, T. S. Chan, L. Y. Chang and X. Fan, *Small*, 2024, **20**, e2400564.
117 F. She, Z. Guo, F. Liu, Z. Yu, J. Chen, Y. Fan, Y. Lei, Y. Chen, H. Li and L. Wei, *ACS Catal.*, 2024, **14**, 10928–10938.
118 P. Cao, X. Quan, X. Nie, K. Zhao, Y. Liu, S. Chen, H. Yu and J. G. Chen, *Nat. Commun.*, 2023, **14**, 172.
119 Z. Deng, S. J. Choi, G. Li and X. Wang, *Chem. Soc. Rev.*, 2024, **53**, 8137–8181.
120 M. R. Gerhardt, A. A. Wong and M. J. Aziz, *J. Electrochem. Soc.*, 2018, **165**, A2625–A2643.
121 Y. Chen, C. Zhen, Y. Chen, H. Zhao, Y. Wang, Z. Yue, Q. Wang, J. Li, M. D. Gu, Q. Cheng and H. Yang, *Angew. Chem., Int. Ed.*, 2024, **63**, e202407163.
122 S. Subramanian, K. Yang, M. Li, M. Sassenburg, M. Abdinejad, E. Irtem, J. Middelkoop and T. Burdyny, *ACS Energy Lett.*, 2023, **8**, 222–229.
123 D. Corral, J. T. Feaster, S. Sobhani, J. R. DeOtte, D. U. Lee, A. A. Wong, J. Hamilton, V. A. Beck, A. Sarkar, C. Hahn, T. F. Jaramillo, S. E. Baker and E. B. Duoss, *Energy Environ. Sci.*, 2021, **14**, 3064–3074.
124 J. Li, Z. Wang, S. Liu, Z. Chen, J. Yang, Z. Chen, A. Li, Q. Wen, L. Wang, S. Qiu, C. Cui, H. Deng and F. Deng, *Chem. Eng. J.*, 2024, **481**, 148452.
125 S. Jia, H. Yu, J. Na, Z. Liu, K. Lv, Z. Ren, S. Sun and Z. Shao, *ACS Appl. Mater. Interfaces*, 2024, **16**, 23099–23108.
126 B. N. Ruggiero, X. K. Lu, K. Adonteng, J. Dong, J. M. Notestein and L. C. Seitz, *Chem. Eng. J.*, 2024, **486**, 150246.
127 L. Fan, Y. Zhao, L. Chen, J. Chen, J. Chen, H. Yang, Y. Xiao, T. Zhang, J. Chen and L. Wang, *Nat. Catal.*, 2023, **6**, 585–595.
128 P. C. Foller and R. T. Bombard, *J. Appl. Electrochem.*, 1995, **25**, 613–627.
129 Z. Chen, S. Chen, S. Siahrostami, P. Chakthranont, C. Hahn, D. Nordlund, S. Dimosthenis, J. K. Nørskov, Z. Bao and T. F. Jaramillo, *React. Chem. Eng.*, 2017, **2**, 239–245.
130 J. Qi, Y. Du, Q. Yang, N. Jiang, J. Li, Y. Ma, Y. Ma, X. Zhao and J. Qiu, *Nat. Commun.*, 2023, **14**, 6263.
131 Y. Sun, K. Fan, J. Li, L. Wang, Y. Yang, Z. Li, M. Shao and X. Duan, *Nat. Commun.*, 2024, **15**, 6098.
132 E. Berl, *Trans. Electrochem. Soc.*, 1939, **76**, 359.
133 G. A. Truesdale and A. L. Downing, *Nature*, 1954, **173**, 1236.
134 T. Kinumoto, M. Inaba, Y. Nakayama, K. Ogata, R. Umebayashi, A. Tasaka, Y. Iriyama, T. Abe and Z. Ogumi, *J. Power Sources*, 2006, **158**, 1222–1228.
135 J. Li and H. Duan, *Chem*, 2024, **10**, 1–32.
136 H. Sheng, A. N. Janes, R. D. Ross, H. Hofstetter, K. Lee, J. R. Schmidt and S. Jin, *Nat. Catal.*, 2022, **5**, 716–725.
137 S.-K. Geng, Y. Zheng, S.-Q. Li, H. Su, X. Zhao, J. Hu, H.-B. Shu, M. Jaroniec, P. Chen, Q.-H. Liu and S.-Z. Qiao, *Nat. Energy*, 2021, **6**, 904–912.
138 J. Wang, X. Liu, C. Ma, H. Fu, S. Chen, N. Li, Y. Li, X. Fan and W. Peng, *Chem Catal.*, 2024, **4**, 101090.
139 L. Li, C. Tang, Y. Zheng, B. Xia, X. Zhou, H. Xu and S. Z. Qiao, *Adv. Energy Mater.*, 2020, **10**, 2000789.
140 K. Dong, J. Liang, Y. Wang, Y. Ren, Z. Xu, H. Zhou, L. Li, Q. Liu, Y. Luo, T. Li, A. M. Asiri, Q. Li, D. Ma and X. Sun, *Chem Catal.*, 2021, **1**, 1437–1448.
141 Z. Wang, X. Duan, M. G. Sendeku, W. Xu, S. Chen, B. Tian, W. Gao, F. Wang, Y. Kuang and X. Sun, *Chem Catal.*, 2023, **3**, 100672.
142 C. Xia, S. Back, S. Ringe, K. Jiang, F. Chen, X. Sun, S. Siahrostami, K. Chan and H. Wang, *Nat. Catal.*, 2020, **3**, 125–134.
143 K. Otsuka and I. Yamanaka, *Electrochim. Acta*, 1990, **35**, 319–322.
144 I. Yamanaka, S. Tazawa, T. Murayama, R. Ichihashi and N. Hanaizumi, *ChemSusChem*, 2008, **1**, 988–992.
145 I. Yamanaka, S. Tazawa, T. Murayama, T. Iwasaki and S. Takenaka, *ChemSusChem*, 2010, **3**, 59–62.
146 W. Li, A. Bonakdarpour, E. Gyenge and D. P. Wilkinson, *ChemSusChem*, 2013, **6**, 2137–2143.
147 C. Xia, Y. Xia, P. Zhu, L. Fan and H. Wang, *Science*, 2019, **366**, 226–231.
148 W. Wang, Y. Hu, Y. Liu, Z. Zheng and S. Chen, *ACS Appl. Mater. Interfaces*, 2018, **10**, 31855–31859.
149 H. Li, P. Wen, D. S. Itanze, Z. D. Hood, S. Adhikari, C. Lu, X. Ma, C. Dun, L. Jiang, D. L. Carroll, Y. Qiu and S. M. Geyer, *Nat. Commun.*, 2020, **11**, 3928.
150 J. Yang, R. Ding, C. Liu, Q. Xu, S. Liu and X. Yin, *J. Phys.: Energy*, 2024, **6**, 015022.
151 G. Merle, M. Wessling and K. Nijmeijer, *J. Membr. Sci.*, 2011, **377**, 1–35.
152 R. Xie, C. Cheng, R. Wang, J. Li, E. Zhao, Y. Zhao, Y. Liu, J. Guo, P. Yin and T. Ling, *ACS Catal.*, 2024, **14**, 4471–4477.
153 T. Lu, M. Sun, F. Wang, S. Chen, Y. Li, J. Chen, X. Liao, X. Sun, Y. Liu, F. Wang, B. Huang and H. Wang, *ACS Nano*, 2024, **18**, 15035–15045.
154 H. Sheng, R. D. Ross, J. R. Schmidt and S. Jin, *ACS Energy Lett.*, 2023, **8**, 196–212.
155 Y. Wang, C. Han, L. Ma, T. Duan, Y. Du, J. Wu, J.-J. Zou, J. Gao, X.-D. Zhu and Y.-C. Zhang, *Small*, 2024, **20**, 2309448.
156 Y. Bu, R. Ma, Y. Wang, Y. Zhao, F. Li, G.-F. Han and J.-B. Baek, *Adv. Mater.*, 2024, **36**, 2412670.
157 C. He, C. Xia, F.-M. Li, J. Zhang, W. Guo and B. Y. Xia, *Adv. Energy Mater.*, 2024, **14**, 2303233.
158 Y. Li, D. Luan and X. W. Lou, *Adv. Mater.*, 2024, **36**, 2412386.
159 M. Deng, D. Wang and Y. Li, *Adv. Mater.*, 2024, **36**, 2314340.
160 Y.-Y. Yan, W.-J. Niu, W.-W. Zhao, R.-J. Li, E.-P. Feng, B.-X. Yu, B.-K. Chu and C.-Y. Cai, *Adv. Energy Mater.*, 2024, **14**, 2303506.
161 L. Zhao, R. Yan, B. Mao, R. Paul, W. Duan, L. Dai and C. Hu, *Small*, 2024, **20**, 2403029.
162 M. Mazzucato, A. Facchin, M. Parnigotto and C. Durante, *ACS Catal.*, 2024, **14**, 6369–6403.
163 Y. Zhou, L. Xu, J. Wu, W. Zhu, T. He, H. Yang, H. Huang, T. Cheng, Y. Liu and Z. Kang, *Energy Environ. Sci.*, 2023, **16**, 3526–3533.

164 Y. Yao, H. Wang, K. Dong, H. Li, J. Liang, R. Li, S. Sun, Z. Cai, X. He, D. Zheng, Y. Luo, S. Alfaifi, D. Ma, W. Hu and X. Sun, *J. Mater. Chem. A*, 2023, **11**, 22154–22160.

165 S. Ding, B. Xia, M. Li, F. Lou, C. Cheng, T. Gao, Y. Zhang, K. Yang, L. Jiang, Z. Nie, H. Guan, J. Duan and S. Chen, *Energy Environ. Sci.*, 2023, **16**, 3363–3372.

166 Q. Huang, B. Xia, M. Li, H. Guan, M. Antonietti and S. Chen, *Nat. Commun.*, 2024, **15**, 4157.

167 S. Ding, Y. Zhang, F. Lou, M. Li, Q. Huang, K. Yang, B. Xia, C. Tang, J. Duan, M. Antonietti and S. Chen, *Mater. Today Energy*, 2023, **38**, 101430.

168 V. Alvarado-Pérez, L. I. Cabrera-Lara, G. López-Téllez, D. Mendoza-Anaya, S. Hernández-López and M. Camacho-López, *Mater. Chem. Phys.*, 2019, **233**, 180–184.

169 X. Zhou, Y. Min, C. Zhao, C. Chen, M.-K. Ke, S.-L. Xu, J.-J. Chen, Y. Wu and H.-Q. Yu, *Nat. Commun.*, 2024, **15**, 193.

170 J. Xu, X. Zheng, Z. Feng, Z. Lu, Z. Zhang, W. Huang, Y. Li, D. Vuckovic, Y. Li, S. Dai, G. Chen, K. Wang, H. Wang, J. K. Chen, W. Mitch and Y. Cui, *Nat. Sustainability*, 2021, **4**, 233–241.

171 X. Cheng, X. Jiang, S. Yin, L. Ji, Y. Yan, G. Li, R. Huang, C. Wang, H. Liao, Y. Jiang and S. Sun, *Angew. Chem., Int. Ed.*, 2023, **62**, e202306166.

172 H. Xie, X. Xie, G. Hu, V. Prabhakaran, S. Saha, L. Gonzalez-Lopez, A. H. Phakatkar, M. Hong, M. Wu, R. Shahbazian-Yassar, V. Ramani, M. I. Al-Sheikhly, D.-E. Jiang, Y. Shao and L. Hu, *Nat. Energy*, 2022, **7**, 281–289.

173 C. Ni, Z. Fan, N. Deng and X. Huang, *ACS Appl. Energy Mater.*, 2024, **7**, 3116–3124.

174 H. Huang, Z. Zhong, J. Li and H. Li, *ACS Appl. Energy Mater.*, 2024, **7**, 10804–10814.

175 M. S. Enstrup, J. Steinmann, F. G. Daragan, B. Dangpiaei and U. Kunz, *ChemSusChem*, 2024, **17**, e202400491.

176 H. Nguyen, C. Klose, L. Metzler, S. Vierrath and M. Breitwieser, *Adv. Energy Mater.*, 2022, **12**, 2103559.

177 H. Zhang and P. K. Shen, *Chem. Rev.*, 2012, **112**, 2780–2832.

178 D. W. Shin, M. D. Guiver and Y. M. Lee, *Chem. Rev.*, 2017, **117**, 4759–4805.

179 M. Adamski, N. Peressin and S. Holdcroft, *Mater. Adv.*, 2021, **2**, 4966–5005.

180 F. Liu and K. Miyatake, *J. Mater. Chem. A*, 2022, **10**, 7660–7667.

181 F. Akinori, S. Hironori and T. Takashi, *Comput. Theor. Chem.*, 2017, **1121**, 44–48.

182 W. Li, Y. Xie, L. Chen, Z. Lin, Z. Zhao, G. Chen, J. Pang and Z. Jiang, *J. Membr. Sci.*, 2024, **706**, 122952.

183 C. P. Gordon, H. Engler, A. S. Tragl, M. Plodinec, T. Lunkenbein, A. Berkessel, J. H. Teles, A.-N. Parvulescu and C. Copéret, *Nature*, 2020, **586**, 708–713.

184 Q. Jiang, Y. Ji, T. Zheng, X. Li and C. Xia, *ACS Mater. Au*, 2024, **4**, 133–147.

185 X. Li, K. Wu, S. Chen, B. Yuan, J. Wang, C. Tang and Q. Zhang, *Chem Catal.*, 2024, **4**, 100997.

186 M. H. Guan, T. Wu and A. H. Lu, *ChemCatChem*, 2023, **15**, e202301311.

187 D. Pollok and S. R. Waldvogel, *Chem. Sci.*, 2020, **11**, 12386–12400.

188 H. Zhang, S. Wu, X. Huang, L. Li, Q. Liao and Z. Wei, *Chem. Eng. J.*, 2022, **428**, 131534.

189 Q. Jiang, Y. Ji, T. Zheng, X. Li and C. Xia, *ACS Mater. Au*, 2024, **4**, 133–147.

190 X.-C. Liu, W.-K. Yao, B.-Y. Su, Y.-H. Hong, T. Wang, Z.-Y. Zhou and S.-G. Sun, *Electrochem. Commun.*, 2023, **151**, 107510.

191 C. H. Yang, X. C. Liu, Y. Li, S. Yuan, T. Wang, Z. Y. Zhou and S. G. Sun, *ChemSusChem*, 2023, **16**, e202300699.

192 X. Jiang, R. Chen, Y.-X. Chen and C.-Z. Lu, *Chem. Synth.*, 2024, **4**, 4–6.

193 C. Y. Chen, C. Tang, H. F. Wang, C. M. Chen, X. Zhang, X. Huang and Q. Zhang, *ChemSusChem*, 2016, **9**, 1194–1199.

194 X. Meng, X. Cui, N. P. Rajan, L. Yu, D. Deng and X. Bao, *Chem*, 2019, **5**, 2296–2325.

195 J. Kim, J. H. Kim, C. Oh, H. Yun, E. Lee, H. S. Oh, J. H. Park and Y. J. Hwang, *Nat. Commun.*, 2023, **14**, 4704.

196 S. Chen, S. Liang, R. Huang, M. Zhang, Y. Song, Y. Zhang, S. Tao, L. Yu and D. Deng, *Nat. Synth.*, 2023, **3**, 76–84.

197 Y. Yuan, L. Chen, Z. Wan, K. Shi, X. Teng, H. Xu, P. Wu and J. Shi, *Sci. Adv.*, 2024, **10**, eado1755.

198 Y. Li, W. Cao and X. Zuo, *Environ. Res.*, 2022, **212**, 113508.

199 X. Qin, K. Zhao, X. Quan, P. Cao, S. Chen and H. Yu, *J. Hazard. Mater.*, 2021, **416**, 125859.

200 Z. Lin, Felice, G. E. P. O'Connell, T. Wan, D. Zhang, L. Peng, D. Chu, X. Lu and Z. Han, *Chem. Eng. J.*, 2024, **481**, 148736.

201 E. Brillas, I. Sirés and M. A. Oturan, *Chem. Rev.*, 2009, **109**, 6570–6631.

202 M. H. Guan, L. Y. Dong, T. Wu, W. C. Li, G. P. Hao and A. H. Lu, *Angew. Chem., Int. Ed.*, 2023, **62**, e202302466.

203 B. N. Ruggiero, A. R. Weidner, J. M. Notestein and L. C. Seitz, *J. Phys. Chem. C*, 2023, **127**, 20640–20651.

204 B. N. Ruggiero, K. M. Sanroman Gutierrez, J. D. George, N. M. Mangan, J. M. Notestein and L. C. Seitz, *J. Catal.*, 2022, **414**, 33–43.

205 X. Kong, C. Liu, Z. Xu, J. Zhao, J. Ni, H. Li, T. Zheng, C. Xia, Z. Geng and J. Zeng, *Angew. Chem., Int. Ed.*, 2024, e202411160, DOI: 10.1002/anie.202411160.